Title: In Vivo Reporter of Endolysosomal Lipids Reveals Enduring Effects of Diet on Hepatic Macrophages

Authors: Thomas V. Galassi[1,2], Prakrit V. Jena[1], Janki Shah[1], Geyou Ao[3], Elizabeth Molitor[4], Yaron Bram[2], Angela Frankel[2], Jiwoon Park[2], Jose Jessurun[2], Daniel S. Ory[4], Adriana Haimovitz-Friedman[1], Daniel Roxbury[5], Jeetain Mittal[6], Ming Zheng[3], Robert E. Schwartz[2], Daniel A. Heller[1,2*]

Affiliations:
[1]Memorial Sloan Kettering Cancer Center, New York, NY 10065

[2]Weill Cornell Medicine, New York, NY 10065

[3]National Institute of Standards and Technology, Gaithersburg, MD 20899

[4]Department of Medicine, Washington University School of Medicine, St. Louis, MO 63110

[5]Department of Chemical Engineering, University of Rhode Island, Kingston, RI 02881

[6]Department of Chemical and Biomolecular Engineering, Lehigh University, Bethlehem, PA 18015

*Corresponding author. Email: hellerd@mskcc.org

Abstract: The abnormal accumulation of lipids within the endolysosomal lumen occurs in many conditions, including lysosomal storage disorders and non-alcoholic fatty liver disease (NAFLD). Current technologies cannot monitor endolysosomal lipid content *in vivo*, hindering drug development and our understanding of NAFLD pathophysiology. We developed a carbon nanotube-based optical reporter that non-invasively measures endolysosomal lipid accumulation *in vivo via* bandgap modulation of its intrinsic near-infrared emission. The reporter detected lipid accumulation in live Niemann-Pick disease, atherosclerosis, and non-alcoholic steatohepatitis (NASH) models. Using the technology, we discovered endolysosomal lipid accumulation in hepatic macrophages in early stages of progression towards NASH. Elevated lipid levels also persist long after reverting to a normal diet, suggesting that dietary changes induce long-term modulation of hepatic macrophage physiology towards a NASH phenotype.

One Sentence Summary: In vivo detection of endolysosomal lipids reveals changes in hepatic macrophage physiology during NASH development.

Main Text: The accumulation of lipids in endolysosomal organelles has been implicated in diverse pathologies including neurodegenerative diseases (*1*), lysosomal storage disorders (*2*), atherosclerosis (*3*), non-alcoholic fatty liver disease (NAFLD) (*3*), and drug induced phospholipidosis (DIPL) (*4*). However, current methods for the *in vivo* detection of endolysosomal lipid accumulation are lacking. While techniques such as magnetic resonance imaging, magnetic resonance spectroscopy, positron emission topography, computer tomography, nuclear magnetic resonance spectroscopy, ultrasound, and dual energy X-ray absorptiometry have been effectively used in the clinic to quantify lipid content in specific organs or tissues, they show no specificity for individual organelles (*5*). Similarly, optical coherence tomography (*6*) and intracoronary near-infrared (NIR) spectroscopy (*7*) can detect lipid rich atherosclerotic plaques *in vivo*, but these methods also do not provide information on the lipid content of specific organelles. Transmission electron microscopy (TEM), while appropriate for the visualization of lipid accumulation within endolysosomal organelles (*8*), is expensive, time consuming, only applicable for resected tissues, and gives qualitative and subjective results (*9*). Experimental probes with the ability to non-invasively monitor lipid flux or accumulation in endolysosomal organelles in *in vivo* animal models do not currently exist.

A non-invasive method to detect endolysosomal lipid accumulation *in vivo* would aid in the investigation of disease pathogenesis. In the study of NAFLD, a spectrum of disorders affecting over 30 % of the general population (*10*), past work suggests that the accumulation of endolysosomal lipids in Kupffer cells (KCs), the resident liver macrophages, may be implicated in disease progression towards non-alcoholic steatohepatitis (NASH) (*11, 12*). NASH is a progressive form of NAFLD that is characterized by the concurrent presence of hepatic steatosis and inflammation, and may lead to fibrosis, cirrhosis or hepatocellular carcinoma (*10, 13*).

Despite the negative health effects associated with the progression of early stage NAFLD to NASH, the underlying mechanisms remain poorly understood, and the relationship between KC endolysosomal lipid accumulation and disease progression has not been extensively studied. This is due in part to a lack of methods to monitor KC endolysosomal lipid flux or accumulation in live animals. Such a method would serve as a valuable tool in the elucidation of NAFLD/NASH pathogenesis.

A method to non-invasively assess the accumulation of lipids in endolysosomal organelles *in vivo* would be important in the context of drug development for NAFLD and lysosomal storage disorders. Such a method would allow for the *in vivo* efficacy of candidate compounds to be assessed rapidly and non-invasively in animal models, making the drug discovery process more efficient. Such a method would also be directly applicable to the assessment of drug-induced phospholipidosis (DIPL), a condition characterized by the accumulation of drug, phospholipid, and cholesterol in the lysosomal lumen of cells (*4*, *14*) that has been recognized by the FDA as a major regulatory concern that impedes the drug development process (*4, 15, 16*). When assessing candidate compounds, pharmaceutical companies frequently assess DIPL *in vivo*, with TEM serving as the gold standard of detection methods (*14*). A technique that quantitatively, rapidly, and non-invasively assesses endolysosomal lipid accumulation *in vivo* could replace TEM measurements in the identification of DIPL, streamlining the drug development process.

Here, we present an optical reporter that non-invasively monitors endolysosomal lipid accumulation and flux from within KCs *in vivo*. The reporter localizes within endolysosomal organelles of KCs rapidly upon intravenous injection. The reporter can be monitored *in vivo* via near-infrared excitation/emission through the animal non-invasively. We detected hepatic lipid

accumulation within well-established animal models of the lysosomal lipid storage diseases Niemann-Pick Disease type A/B (NPA/B) and Niemann-Pick Disease type C (NPC). We also found that the reporter dynamically and longitudinally monitors the accumulation of lipids in KC endolysosomal organelles over a period of minutes upon administration of oxidized low density lipoprotein (oxLDL) and over several weeks in a model of NAFLD/NASH. We found that the KC endolysosomal lipid accumulation benchmarks NAFLD progression towards NASH, and that lipid accumulation is visible at early timepoints (within two weeks of initiation of a high fat, high fructose diet). We also found that the accumulation persists long after resuming a normal diet, suggesting that Kupffer cell physiology is significantly modified by even a relatively small change in diet.

RESULTS

Reporter development and characterization

To develop an *in vivo* reporter of KC endolysosomal lipid accumulation, we utilized the intrinsic near infrared fluorescence from a structurally sorted single-walled carbon nanotube (SWCNT) that was non-covalently complexed with single-stranded (ss) DNA (DNA-SWCNT). This built on past work by our group demonstrating that DNA-SWCNTs localize to endolysosomal organelles where they can detect lipid accumulation *in vitro* without adversely affecting organelle size, shape, integrity, capacity to digest lipoproteins; or cell viability, or proliferation (*17*).

A population of SWCNTs contains discrete structural species (chiralities) that differ in diameter and chiral angle (*18*). These discrete chiralities are identified by the chiral integers (n,m) (*18*), and semiconducting SWCNT chiralities are intrinsically fluorescent in the near-

infrared region of the spectrum (*19*). We assessed the potential of several DNA-sequence nanotube chirality combinations to serve as a potential reporter of endolysosomal lipid accumulation *in vivo* (fig. S1). In solution each of the tested combinations exhibited a >9 nm decrease in emission center wavelength in response to 0.5 mg/mL low density lipoprotein (LDL) (fig. S2A). When internalized by cells exhibiting endolysosomal lipid accumulation, each tested combination once again exhibited a decrease in emission center wavelength, with ssCTTC$_3$TTC-(9,4) showing the greatest decrease (fig. S2B). The emission wavelength of ssCTTC$_3$TTC-(9,4) was also found to be minimally affected by a decrease in pH, highlighting its potential as a reporter of lipid accumulation in endolysosomal organelles *in vivo* (fig. S3).

The ssCTTC$_3$TTC-(9,4) construct, which builds off of the previously employed reporter for endolysosomal lipid accumulation *in vitro (17)*, is a second-generation nanomaterial engineered for *in vivo* applications. It is purified through a recently developed aqueous two phase polymer separation (ATP) method (*20*), rather than through ion-exchange high performance liquid chromatography (IEX-HPLC) (*21*), which is used to purify the *in vitro* reporter (*17*). Unlike IEX-HPLC, the ATP separation method is an inexpensive, highly scalable process that allows for the production of the quantities of structurally sorted SWCNT needed for thorough *in vivo* studies with multiple biological replicates (*22*). Moreover, unlike the previously employed reporter, ssCTTC$_3$TTC-(9,4) emits in the (1110 to1150) nm range, which is ideal for non-invasive detection through biological tissue (*23*, *24*).

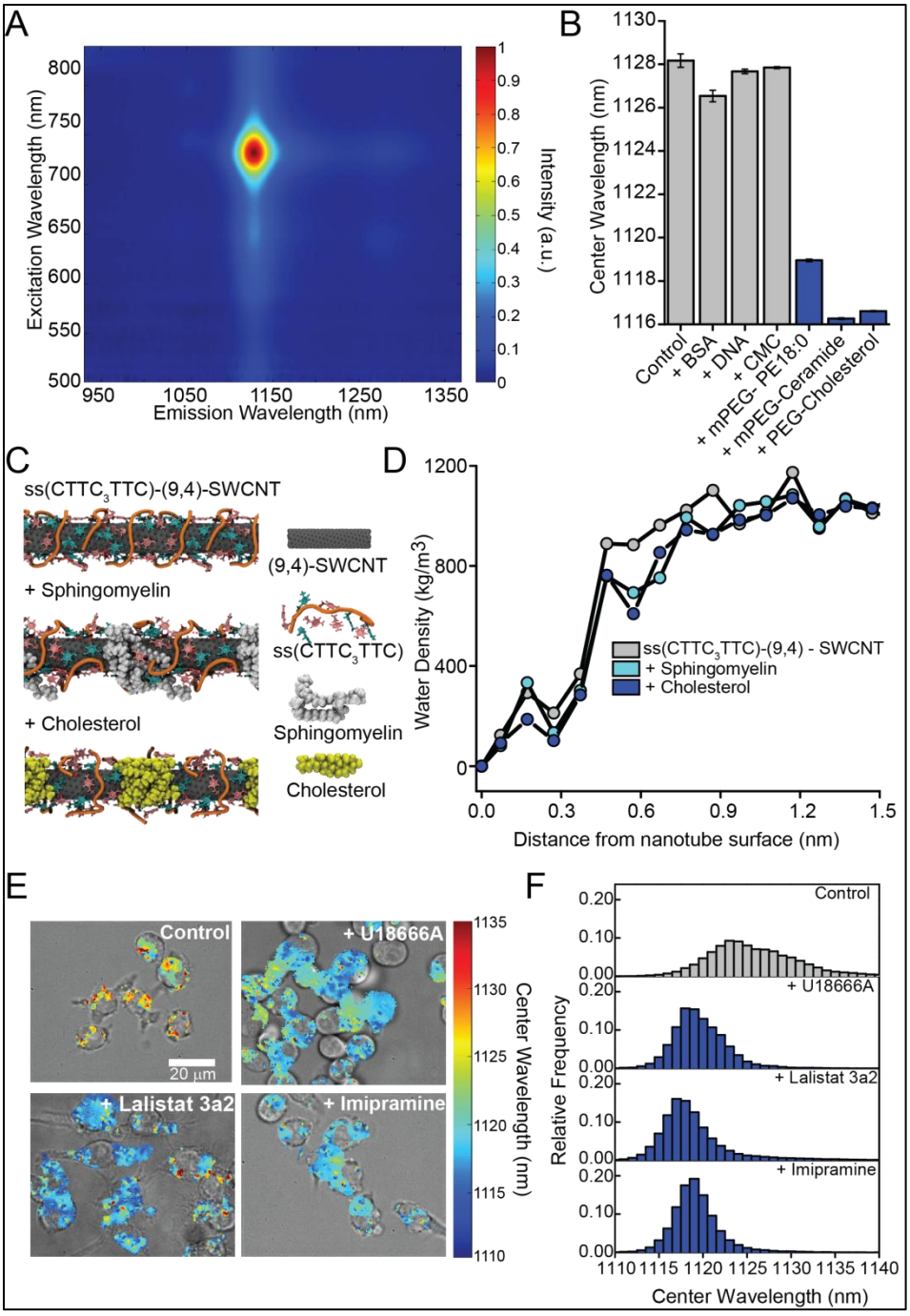

Fig. 1. Characterization of the ssCTTC$_3$TTC-(9,4) optical reporter. (A) Photoluminescence excitation emission plot of ssCTTC$_3$TTC-(9,4). **(B)** Nanotube emission center wavelength +/- standard deviation in cell culture media with 1% FBS at near saturating concentrations of bovine serum albumin (BSA, 20 mg/mL) salmon testes dsDNA (1 mg/mL), carboxymethyl cellulose (CMC, 5 mg/mL), as well as mPEG-phosphoethanolamine 18:0 (mPEG-PE 18:0, 5.93 mmol/L) PEG-cholesterol (5.93 mmol/L), and mPEG-ceramide (5.93 mmol/L). Error bars represent standard deviation

from n = 3 technical replicates. **(C)** Frames from molecular dynamics simulations showing equilibrated structures of the ssCTTC$_3$TTC-(9,4) nanotube complex in the presence of cholesterol and sphingomyelin. **(D)** Water density as a function of distance from the surface of ssCTTC$_3$TTC-(9,4) nanotube complexes, in the presence of sphingomyelin or cholesterol, or with no lipids present. **(E)** Overlays of transmitted light and hyperspectral images of the reporter in RAW 264.7 macrophages cultured in complete cell culture media, and in complete cell culture media supplemented with U18666A (3 µg/mL), Lalistat 3a2 (10 µmol/L), or imipramine hydrochloride (10 µmol/L). **(F)** Histogram of emission center wavelengths from all pixels with NIR emission from the hyperspectral images of cells under the conditions described in (E).

After identifying ssCTTC$_3$TTC-(9,4) as a potential reporter of endolysosomal lipid accumulation *in vivo*, we characterized its optical response in a biologically relevant environment *in vitro*. Following acquisition of a protein corona, acquired *via* incubation in cell culture media with 1 % fetal bovine serum (FBS) for 90 min, the reporter had an excitation maximum at 732 nm, and an emission maximum at 1128 nm (Fig. 1A). When exposed to various classes of biomolecules and water-soluble lipid analogs, the reporter showed minimal response to near saturating concentrations of bovine serum albumin (BSA), genomic DNA, and carboxymethyl cellulose (CMC), but exhibited an (6 to 8) nm decrease in emission center wavelength (herein described as a "blue shift") in response to the water-soluble lipid analogs polyethylene glycol (PEG)-cholesterol, methoxy PEG (mPEG)-ceramide (C16), and mPEG-phosphoethanolamine (18:0) (Fig. 1B, fig. S4). The median length of the reporter as measured *via* atomic force microscope, was 133 nm (fig. S5).

To better understand the reporter's mechanism of detection we conducted all atom replica exchange molecular dynamics simulations. Similar to what was seen in a previous study (*17*), simulations suggested that sphingomyelin or cholesterol molecules bind to the reporter surface *via* hydrophobic interactions, decreasing the water density in the nanotube's immediate vicinity

(Fig. 1C-D, fig. S6-7). This likely leads to an effective decrease of the local solvent dielectric, resulting in the observed blue shift (*17*).

Reporter validation in live cells

Following *in silico* and *in vitro* characterization of the reporter, its functionality in live cells was validated. Endolysosomal lipid accumulation was induced in RAW 264.7 macrophages *via* three distinct mechanisms - cells were treated with U18666A, Lalistat 3a2, or imipramine hydrochloride. Treatment with U18666A is known to mimic the lysosomal storage disorder NPC by inhibiting the Niemann-Pick C1 (NPC1) protein (*25*), which causes the accumulation of unesterified cholesterol in lysosomes (*26*). Lalistat 3a2 inhibits the enzyme lysosomal acid lipase (LAL) (*27*) and causes a phenotype similar to that seen in Wolman's disease, where LAL deficiency causes an accumulation of esterified cholesterol in lysosomes (*28*). Finally, treatment with imipramine hydrochloride inhibits the enzyme acid sphingomyelinase, causing the accumulation of sphingomyelin in lysosomes similar to what is seen in NPA/B disease (*29*). Following treatment with each inhibitor the reporter was incubated with cells as previously described (*17*). Hyperspectral microscopy (*30*) of the reporter from within cells showed a mean emission center wavelength that was 6 nm blue shifted compared to emission from untreated control cells, demonstrating the ability of ssCTTC$_3$TTC-(9,4) to detect endolysosomal lipid accumulation in live cells (Fig. 1E-F, fig. S8-9).

Reporter biodistribution in vivo

After validating the reporter's ability to detect endolysosomal lipid accumulation *in vitro*, we investigated its biodistribution *in vivo* following intravenous injection. It has long been

established that following intravenous injection, “unprotected” nanoparticles are opsonized and rapidly removed from the blood stream by the macrophages of the reticuloendothelial system, causing the concentration of nanoparticles in the liver and spleen (*31-34*). Moreover, even when somewhat protected from opsonization *via* non-covalent wrapping with PEGylated polymers, SWCNTs have been shown to accumulate in these organs and localize to resident macrophages (*35-37*). We saw similar results with unprotected ssCTTC$_3$TTC-nanotubes as *in vivo* and ex vivo fluorescent measurements showed that nanotubes were rapidly cleared from the blood and localized to the liver following intravenous injection (Fig. 2A-D, supplementary text). The uptake of nanotubes by KCs was confirmed *via* hyperspectral imaging of isolated hepatic cells, demonstrating the potential of the reporter to assess KC endolysosomal lipid accumulation or flux *in vivo* (Fig. 2E, supplementary text).

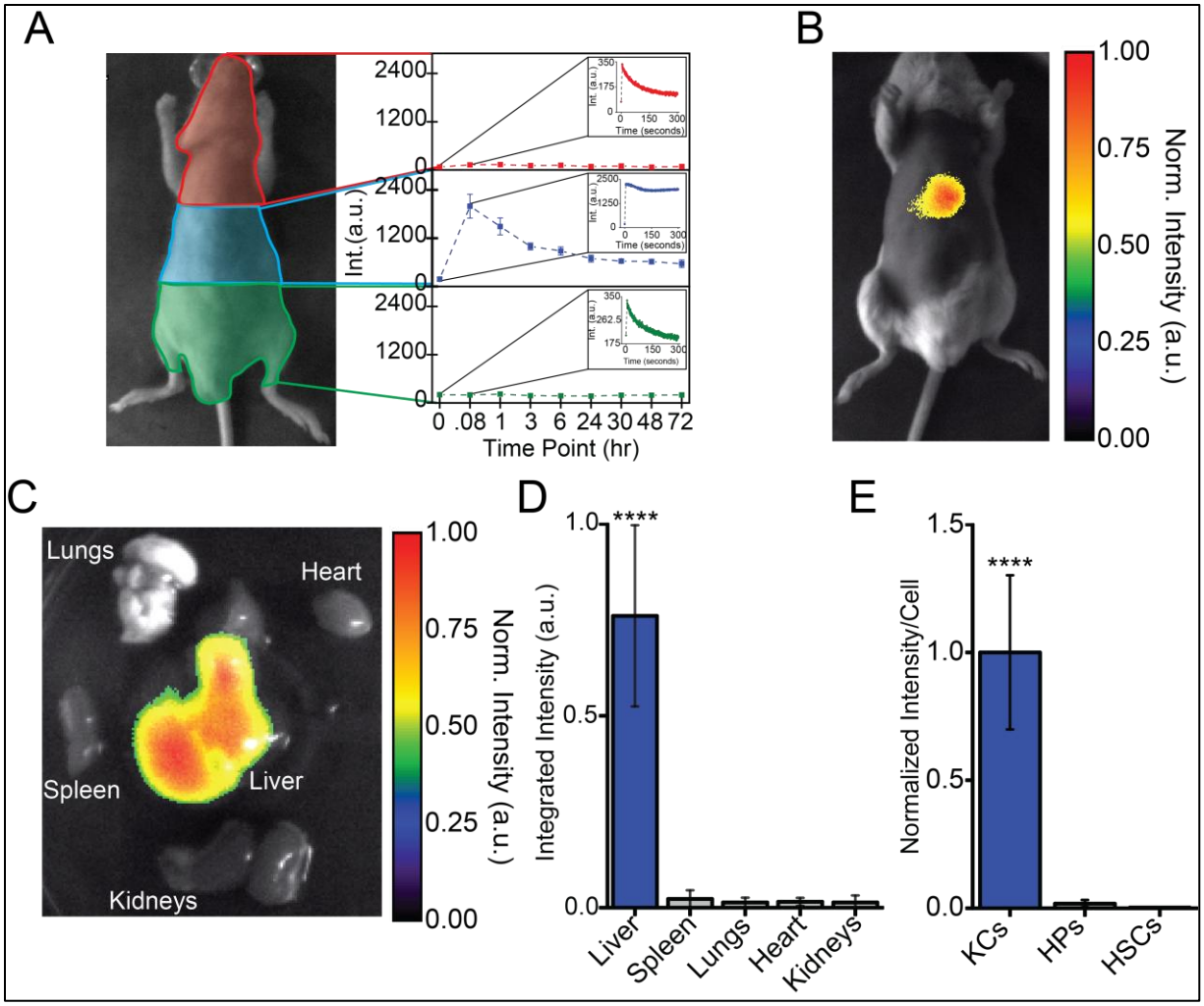

Fig. 2: Reporter biodistribution. (A) Quantification of ssCTTC$_3$TTC-SWCNT fluorescence over time in different regions of mice following intravenous injection. Results are averaged for 5 mice and error bars represent standard deviation. Insets represent the average fluorescence intensity in the specified region immediately following injection. Error bars have been removed for clarity **(B)** Fluorescence image of the reporter *in vivo* 24 h after intravenous injection (200 ng). **(C)** Fluorescence image of the reporter *ex vivo* twenty-four hours after injection. **(D)** Quantification of the reporter's emission spectra *ex vivo* obtained with a near-infrared spectroscope. **** = <.0001 compared to other groups as measured with a one way ANOVA with Dunnet's post test, error bars represent standard deviation. **(E)** Quantification of ssCTTC$_3$TTC-SWCNT emission in isolated Kupffer cells (KCs), hepatocytes (HPs), and hepatic stellate cells (HSCs), following intravenous injection. *** = p<.001 as measured with a one way ANOVA with Tukey's post test, error bars represent standard error of the mean.

Non-invasive detection of lysosomal storage disorders in vivo

The ability of the reporter to non-invasively detect endolysosomal lipid accumulation in KCs *in vivo* was tested using an acid sphingomyelinase knock-out (ASMKO) (*38*) and an NPC1 I1061T ($Npc^{tm(I1061T)Dso}$) knock-in mouse model (*39*). These mouse lines model NPA/B and NPC disease, respectively, and accumulate lipids within the endolysosomal organelles of many cell types, including KCs. To determine if ssCTTC$_3$TTC-(9,4) could detect this accumulation, 200 ng of the reporter was injected intravenously into mice. Reporter emission was then measured non-invasively using a previously described near-infrared *in vivo* spectroscope (*40*) (fig. S10). Compared to wild type (WT) controls, reporter emission from ASMKO and $Npc^{tm(I1061T)Dso}$ mice exhibited an average blue shift of 4.2 nm and 5.3 nm respectively (Fig. 3). This measurement was confirmed using fluorescence spectroscopy ex vivo and *via* hyperspectral microscopy of frozen sections of resected tissue (Fig. 3). The phenotype of each mouse was confirmed *via* histological methods (fig. S11-12).

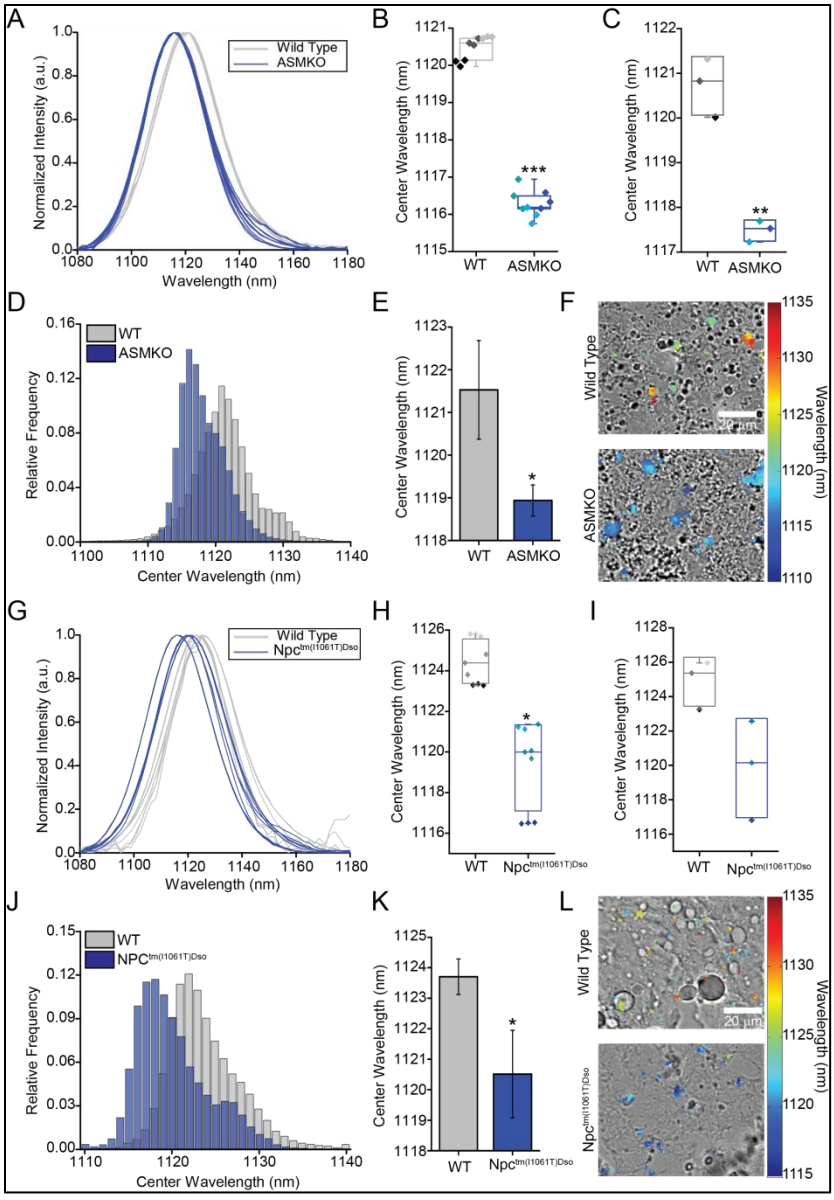

Fig. 3. Non-invasive detection of lysosomal storage disorders *in vivo*. (A) *In vivo* emission spectra of the reporter from live wild type (WT) and acid sphingomyelinase knockout mice (ASMKO) mice. **(B)** Center wavelengths of reporter emission from spectra shown in (A). Diamonds of the same color indicate repeated spectra taken from a single mouse. **(C)** Mean center wavelength of reporter emission taken from the livers of WT and ASMKO mice *ex vivo*. **(D)** Histogram of emission center wavelengths of all pixels from hyperspectral images of frozen sections of resected liver tissue from WT and ASMKO mice. **(E)** Mean center wavelength of reporter emission taken from frozen sections of resected liver tissue with hyperspectral microscopy. **(F)** Overlay of transmitted light and hyperspectral image of nanotube complexes in resected sections of frozen liver tissue from WT and ASMKO mice.

(G) *In vivo* emission spectra of the reporter from live WT and Npc$^{tm(I1061T)Dso}$ mice. **(H)** Center wavelengths of reporter emission from spectra shown in (G). Diamonds of the same color indicate repeated spectra taken from a single mouse. **(I)** Mean center wavelength of reporter emission taken from the livers of WT and Npc$^{tm(I1061T)Dso}$ mice *ex vivo*. **(J)** Histogram of emission center wavelengths of all pixels from hyperspectral images of frozen sections of resected liver tissue from WT and Npc$^{tm(I1061T)Dso}$ mice. **(K)** Mean center wavelength of reporter emission taken from frozen sections of resected liver tissue with hyperspectral microscopy. **(L)** Overlay of transmitted light and hyperspectral image of nanotube complexes in resected sections of frozen liver tissue from WT and Npc$^{tm(I1061T)Dso}$ mice. * = p<.05, ** = p<.01, *** = p<.001, **** = p<.0001 as measured *via* t-test with Welch's correction, N=3 mice per group.

Dynamic detection of oxidized low-density lipoprotein accumulation

We next investigated the ability of the reporter to detect the uptake and endolysosomal accumulation of oxLDL, a process that has been implicated in the development of atherosclerosis and NASH. oxLDL was injected intravenously in mice at doses ranging from (0 to 200) µg, twenty four hours after the injection of 200 ng of the reporter to ensure that any interaction between oxLDL and the reporter occurred in endolysosomal organelles rather than in the circulation (Fig. 4A). Reporter emission from KCs of injected mice was measured non-invasively six hours later and displayed monotonic blue shifting as the injected dose of oxLDL was increased, with a limit of detection between (2 to 20) µg (Fig. 4B). By repeatedly measuring reporter emission at different time points just prior to, and after, oxLDL injection we were able to quantify the kinetics of oxLDL uptake and endolysosomal accumulation by KCs (Fig. 4C). When 200 µg of oxLDL was injected, accumulation could be detected dynamically within 30 min, and a single exponential fit found that the average time constant for this process was 60.63 min (Fig. 4D, fig. S13).

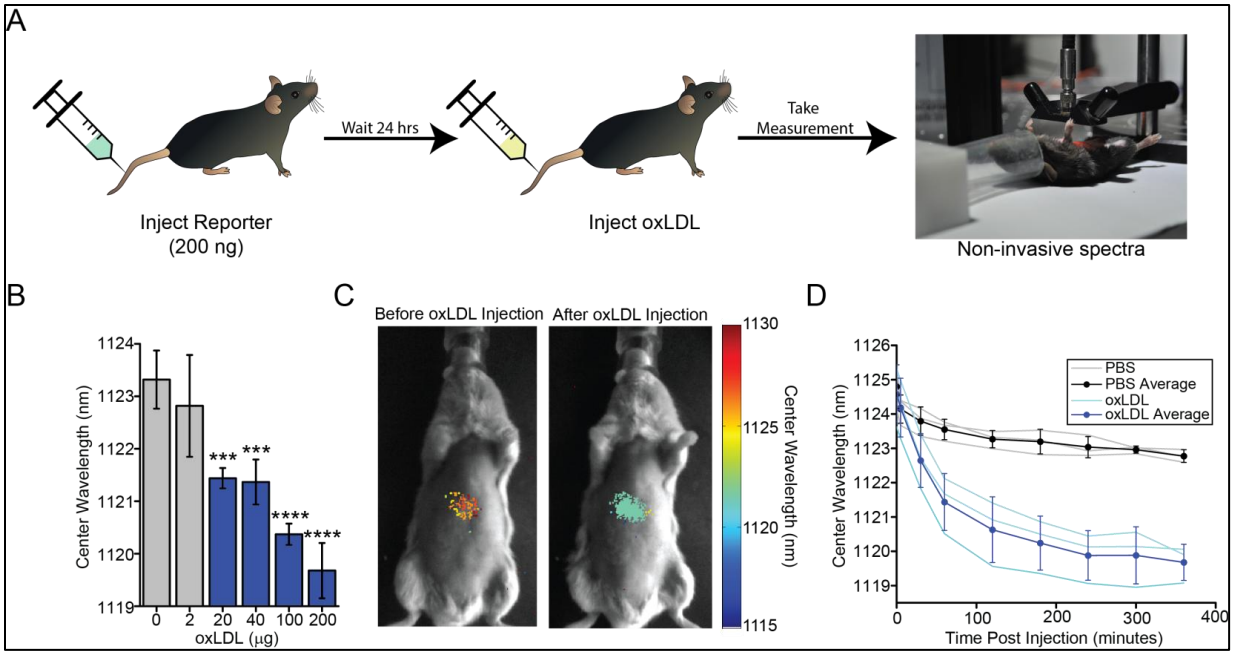

Fig. 4. Dynamic detection of oxidized low-density lipoprotein accumulation. (A) Schematic of experimental procedure used in B-D. **(B)** Mean center wavelength of reporter emission from C57BL/6 mice injected with oxLDL. **(C)** Overlay of transmitted light and hyperspectral image of reporter emission *in vivo* before and after oxLDL injection. **(D)** Trajectories of endolysosomal lipid accumulation from mice injected with 200 μg oxLDL, or PBS. * = p<.05, ** = p<.01, *** = p<.001, **** = p<.0001(all compared to control) as measured with a one way ANOVA with Dunnet's post test, N=3 mice per group. Error bar stands for standard deviation.

Monitoring KC endolysosomal lipids throughout NAFLD progression

Based on previous works (*11*, *12*), we hypothesized that KC endolysosomal lipid accumulation portends NASH development, and that KC endolysosomal lipid accumulation could be used to track NAFLD progression to NASH non-invasively *in vivo*. To test this hypothesis, male C57BL/6 mice were fed standard chow (S.C.) or the Western diet (W.D.) (Envigo 88137) with water supplemented with high fructose corn syrup equivalent for one to three months, as this model has been shown to lead not only to obesity (fig. S14) and steatosis but also NASH development (*41*, *42*). S.C. and W.D. mice were then injected with 200 ng

reporter and nanotube emission was non-invasively measured twenty four hours later. Histological sections showed the presence of macrovesicular steatosis in all W.D. fed mice at each time point, while inflammatory foci were present in all but one mouse after one month of W.D. and in all mice after three months of the W.D. (fig. S15). Results showed that the emission center wavelength of the reporter decreases throughout NAFLD progression towards NASH, indicating an increase in KC endolysosomal lipid accumulation. (Fig. 5A, fig. S16). These results were confirmed *via* ex vivo measurements of excised livers (Fig. 5B). Moreover, S.C. and W.D. fed mice that were injected with the reporter did not show increased liver injury compared to un-injected control mice at the observed time points, as measured *via* histology and serum measurements of the liver injury markers aspartate aminotransferasae, alanine aminotransferase, lactate dehydrogenase, alkaline phosphatase, albumin, globulin, and total protein (fig. S15, S17).

Long term effects of W.D. feeding on KC endolysosomal lipids

The long term effects of W.D. feeding were investigated by altering the diet of mice as described in the previous section for a time period of two weeks. Reporter measurements indicated that this time period was sufficient to induce KC endolysosomal lipid accumulation. Separate groups of mice were then taken off of the W.D. and fed S.C. for two or six additional weeks. Reporter measurements indicated that switching from W.D. to S.C. feeding, even for a time period of six weeks, resulted in only partial reversal of KC endolysosomal lipid accumulation (Fig. 5D). In contrast, histopathologic analysis reveals complete reversal of steatosis and inflammatory changes even within two weeks (Fig. S18). This suggests that a high fat, high fructose diet may have long lasting implications on KC physiology and that these changes are not detectable using standard histiopathologic techniques.

Longitudinal detection of KC endolysosomal lipid accumulation

The ability of the reporter to detect endolysosomal lipid accumulation over time in the same mice was tested by injecting C57BL/6 mice with 100 ng of the reporter intravenously, and measuring the reporter emission wavelength twenty-four hours later. Mice were then fed either S.C. or the W.D. with high fructose corn syrup water for two weeks. A near-infrared *in vivo* spectroscope was then used to verify that signal could not be detected from the first injection of the reporter two weeks prior (mice where signal was noticeable were excluded from further analysis). Mice were then injected with a second dose of the reporter (100 ng), and reporter emission wavelength was measured twenty-four hours later. Results showed that reporter emission in mice had blue shifted over time, but that the magnitude of this blue shifting was significantly greater in mice fed the W.D. for the two week period (Fig. 5E). These results validate the potential of the reporter for use in long term, longitudinal studies; an application with the ability to greatly increase the efficiency and affordability of the drug development process.

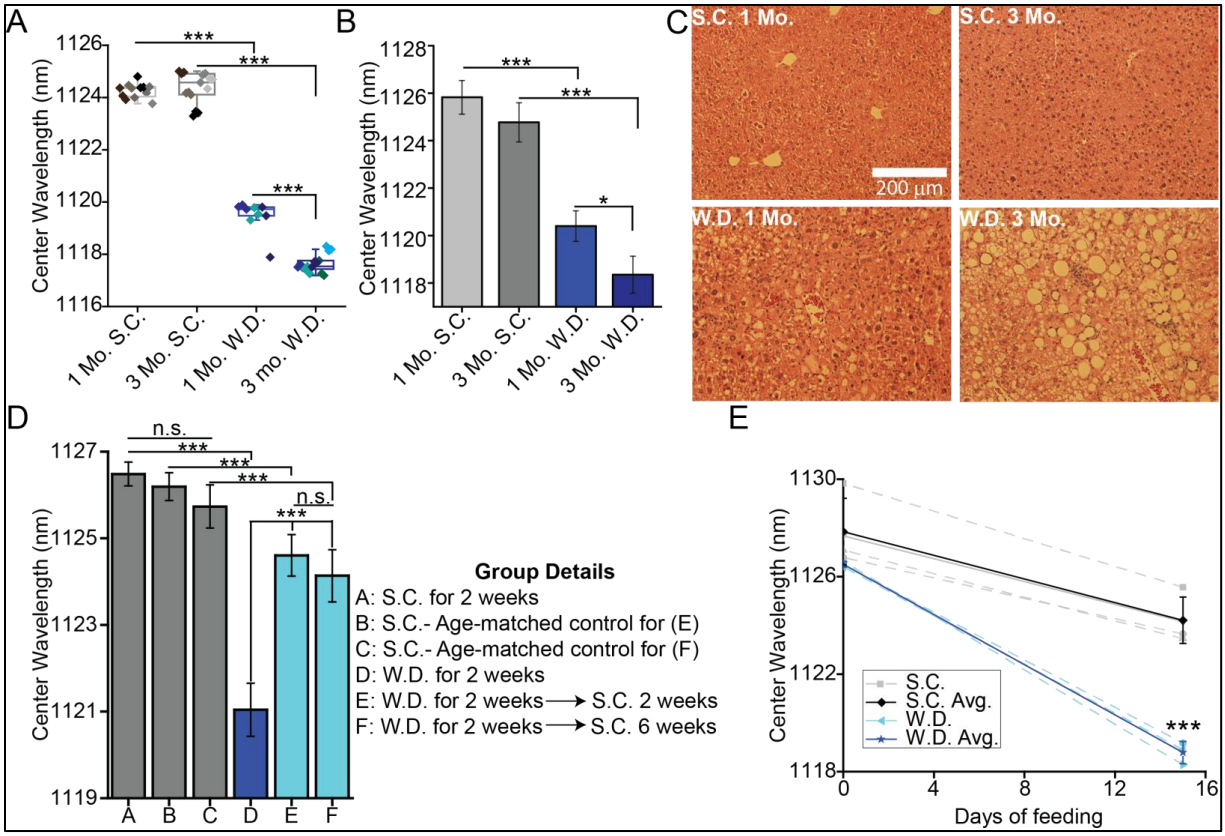

Fig. 5. Tracking NAFLD progression *in vivo*. (A) Center wavelengths of i*n vivo* emission spectra of the reporter from live C57BL/6 mice fed either the Western Diet with high fructose corn syrup-supplemented water (W.D.) or standard chow (S.C.). Diamonds of the same color indicate repeated spectra taken from a single mouse. **(B)** Mean center wavelength of reporter emission taken from the livers of mice *ex vivo*. **(C)** Representative images of H&E stained liver tissue from mice depicted in (A) and (B). **(D)** Mean center wavelength of reporter emission taken from live C57BL/6 mice fed either Western Diet with high fructose corn syrup-supplemented water (W.D.) or standard chow (S.C.) for varying amounts of time. **(E)** Reporter center wavelength in live C57BL/6 mice over time with S.C. or W.D. feeding. Separate injections of reporter were used to obtain signal on day 0 and day 15. *=p<.05, ***=p<.001 as determined with a one way ANOVA with Sidak's post test (A-D), or a t-test with Welch's correction (E), N=(3 to 5) mice per group. Error bar stands for standard deviation.

DISCUSSION

Here, we developed a reporter capable of non-invasive, *in vivo* detection of lipid accumulation in endolysosomal organelles. Using this reporter, we measured endolysosomal

lipid accumulation in hepatic macrophages in early stages of progression towards NASH, and we discovered that elevated lipid levels also persist long after reverting to a normal diet.

The reporter consists of a structurally-purified single-walled carbon nanotube non-covalently complexed with the single stranded oligonucleotide with the sequence $CTTC_3TTC$. This reporter is a second generation nanosensor that was originally engineered to measure endolysosomal lipid accumulation *in vitro* (*17*). Unlike the previously developed reporter which emits in a region where lipids absorb (1200 nm), this reporter has an emission wavelength of 1125 nm, away from the lipid absorption band at 1210 nm (*24*), to facilitate *in vivo* measurements (*23, 24*). To allow the use of the shorter wavelength emission band, separation of the (9,4) nanotube chirality was necessary. This separation process was enabled by the recently developed ATP method (*20*), allowing sufficient quantities of structurally-defined ss$CTTC_3TTC$-(9,4) SWCNT complexes to be isolated for *in vivo* studies.

For Kupffer cell measurements, the reporter localization was likely facilitated by the mononuclear phagocyte system (*33*). When injected intravenously, the reporter accumulated in the liver and localized specifically within Kupffer cells, consistent with multiple studies performed using polymer-wrapped SWCNTs and other classes of non-PEGylated/passivated nanoparticles that can be opsonized within the bloodstream (*31-34*).

The biocompatibility of carbon nanotubes *in vivo* depends on several factors, including the type, size, purity, and functionalization (*43*). For instance, unpurified nanotubes (*44*) and long, multi-walled carbon nanotubes have been implicated in toxicities (*45*). However, several types of non-covalently functionalized single-walled carbon nanotubes are biocompatible across several dose ranges (*36, 37*). By adhering to certain parameters (*44*), carbon nanotube reporters composed of relatively short single-walled carbon nanotubes non-covalently functionalized with

amphiphilic polymers/oligonucleotides have well-documented biocompatibility in live cells (*17, 46*), and animals (*36, 37*). *In vivo*, we conducted several assessments for toxicities, including serum measurements of liver biomarkers and histology measurements. We found that the reporter did not cause or enhance hepatic inflammation or injury in healthy or fatty/steatotic livers.

The reporter measured lipid accumulation specifically within endolysosomal organelles and was applicable to different lipid species. The reporter's response to lipids was assessed against several modified lipids directly in solution, in live cells *via* treatment with chemical inhibitors that promoted accumulation of different compositions (predominantly cholesterol or sphingomyelin), in well-established *in vivo* models of lysosomal storage diseases that also cause accumulation of different lipids, as well as upon intravenous injection of oxidized LDL. Although all lipid species could not be assessed in this manner, the data suggest that it responded generally to lipid accumulation within endosomes/lysosomes. This generality suggests applicability to a range of pathologies, similarly to endolysosomal measurements via electron microscopy, although the nature of the nanosensor allows for *in vivo* assessments, and it does not require tissue processing.

Based on its effectiveness and biocompatibility, we believe that this reporter can be applicable to several types of studies in multiple disease classes. When testing the efficacy of drugs designed to treat lysosomal storage disorders such as NPC disease, researchers must currently rely on the measurement of indirect biomarkers or methods such as TEM, which require the euthanization of animals. Longitudinal assessment of endolysosomal lipid accumulation using the reporter was possible *in vivo* upon repeated administrations in the same

mice over both the short and long term. Use of the reporter in this scenario could improve the speed and reduce animal numbers in certain drug development investigations.

The reporter may also be useful in the development of antibiotic, antidepressant, antipsychotic, antimalarial, and antiarrhythmic drugs, as drugs of these classes often have the side effect of DIPL, which may delay the regulatory process. Companies such as Pfizer (*16*) and Bristol-Meyers Squibb (*4*) have developed risk management strategies to apply to DIPL during the drug development process; however, these strategies rely on indirect biomarkers or TEM to assess the presence of DIPL *in vivo* (*47*), hindering the development of new drugs. We expect that the rapid nature of the method described here will allow for the aforementioned risk management strategies to be streamlined, allowing for a more efficient and cost effective drug development process.

The reporter was also able to dynamically monitor the uptake and accumulation of oxLDL by KCs, a process that began within minutes of oxLDL injection. Further investigation into this process with the reporter may aid in the elucidation of the pathogenesis of atherosclerosis, as oxLDL uptake by Kupffer cells is believed to be a protective mechanism against the formation of atherosclerotic foam cells (*48*).

We used the reporter to study fatty liver disease by examining the relationship between KC endolysosomal lipid accumulation and NAFLD progression. We observed an increase in KC endolysosomal lipid accumulation in the western diet/fructose model. These results support the hypothesis that KC endolysosomal lipid accumulation plays a role in NASH development. We also observed lipid accumulation at early stages (two weeks) on the diet, suggesting that KC endolysosomal lipid accumulation may be a potential early-stage biomarker of NASH development.

We also found that diet-induced KC endolysosomal lipid accumulation persists for at least 6 weeks after the cessation of the high-fat, high-fructose diet. This persistence was not seen using histopathologic techniques. This finding suggests that even small modifications in diet can induce long-term changes in Kupffer cell physiology that may be indicative of a NASH phenotype.

We expect future works using the reporter to investigate a potential mechanistic link between KC endolysosomal lipid accumulation and NASH development. Identification of such a link may aid in the development of NAFLD/NASH therapies and may also potentiate KC endolysosomal lipid accumulation as a biomarker of NASH development.

References and Notes:

1. R. A. Nixon, The role of autophagy in neurodegenerative disease. *Nature medicine* **19**, 983 (2013).
2. A. H. Futerman, G. Van Meer, The cell biology of lysosomal storage disorders. *Nature reviews Molecular cell biology* **5**, 554 (Jul, 2004).
3. T. Hendrikx, S. Walenbergh, M. Hofker, R. Shiri-Sverdlov, Lysosomal cholesterol accumulation: driver on the road to inflammation during atherosclerosis and non-alcoholic steatohepatitis. *obesity reviews* **15**, 424 (May, 2014).
4. L. LeCureux *et al.*, Evaluation and validation of multiple cell lines and primary mouse macrophages to predict phospholipidosis potential. *Toxicology in Vitro* **25**, 1934 (2011).
5. S. B. Heymsfield, H. H. Hu, W. Shen, O. Carmichael, Emerging technologies and their applications in lipid compartment measurement. *Trends in Endocrinology & Metabolism* **26**, 688 (Dec, 2015).
6. T. Kubo *et al.*, Assessment of coronary atherosclerosis using optical coherence tomography. *Journal of atherosclerosis and thrombosis* **21**, 895 (2014).
7. M. Jaguszewski, R. Klingenberg, U. Landmesser, Intracoronary near-infrared spectroscopy (NIRS) imaging for detection of lipid content of coronary plaques: current experience and future perspectives. *Current cardiovascular imaging reports* **6**, 426 (2013).
8. T. Kuemmel, J. Thiele, R. Schroeder, W. Stoffel, Pathology of Visceral Organs and Bone Marrow in an Acid Sphingomyelinase Deficient Knock-Out Mouse Line, Mimicking Human Niemann-Pick Disease Type A: A Light and Electron Microscopic Study. *Pathology-Research and Practice* **193**, 663 (1997).
9. A. M. Schrand, J. J. Schlager, L. Dai, S. M. Hussain, Preparation of cells for assessing ultrastructural localization of nanoparticles with transmission electron microscopy. *nature protocols* **5**, 744 (Apr, 2010).
10. G. Musso, R. Gambino, M. Cassader, Cholesterol metabolism and the pathogenesis of non-alcoholic steatohepatitis. *Progress in lipid research* **52**, 175 (Jan, 2013).
11. V. Bieghs *et al.*, Internalization of modified lipids by CD36 and SR-A leads to hepatic inflammation and lysosomal cholesterol storage in Kupffer cells. *PloS one* **7**, e34378 (2012).
12. V. Bieghs *et al.*, Trapping of oxidized LDL in lysosomes of Kupffer cells is a trigger for hepatic inflammation. *Liver International* **33**, 1056 (Aug, 2013).
13. S. Parekh, F. A. Anania, Abnormal lipid and glucose metabolism in obesity: implications for nonalcoholic fatty liver disease. *Gastroenterology* **132**, 2191 (May, 2007).

14. N. Liu, E. A. Tengstrand, L. Chourb, F. Y. Hsieh, Di-22: 6-bis (monoacylglycerol) phosphate: A clinical biomarker of drug-induced phospholipidosis for drug development and safety assessment. *Toxicology and applied pharmacology* **279**, 467 (2014).
15. B. Berridge *et al.*, Society of Toxicologic Pathology, S., Regulatory Policy Committee Working, G., 2007. Phospholipidosis in nonclinical toxicity studies. *Tox. Path* **35**, 325.
16. L. A. Chatman, D. Morton, T. O. Johnson, S. D. Anway, A strategy for risk management of drug-induced phospholipidosis. *Toxicologic pathology* **37**, 997 (2009).
17. P. V. Jena *et al.*, A Carbon Nanotube Optical Reporter Maps Endolysosomal Lipid Flux. *Acs Nano*, (2017).
18. S. M. Bachilo *et al.*, Structure-assigned optical spectra of single-walled carbon nanotubes. *Science* **298**, 2361 (2002).
19. M. J. O'connell *et al.*, Band gap fluorescence from individual single-walled carbon nanotubes. *Science* **297**, 593 (2002).
20. G. Ao, J. K. Streit, J. A. Fagan, M. Zheng, Differentiating left-and right-handed carbon nanotubes by DNA. *J Am Chem Soc* **138**, 16677 (2016).
21. X. Tu, S. Manohar, A. Jagota, M. Zheng, DNA sequence motifs for structure-specific recognition and separation of carbon nanotubes. *Nature* **460**, 250 (2009).
22. G. Ao, C. Y. Khripin, M. Zheng, DNA-controlled partition of carbon nanotubes in polymer aqueous two-phase systems. *J Am Chem Soc* **136**, 10383 (2014).
23. C.-W. Lin, S. M. Bachilo, M. Vu, K. M. Beckingham, R. B. Weisman, Spectral triangulation: a 3D method for locating single-walled carbon nanotubes in vivo. *Nanoscale* **8**, 10348 (May 21, 2016).
24. C.-L. Tsai, J.-C. Chen, W.-J. Wang, Near-infrared absorption property of biological soft tissue constituents. *Journal of Medical and Biological Engineering* **21**, 7 (2001).
25. F. Lu *et al.*, Identification of NPC1 as the target of U18666A, an inhibitor of lysosomal cholesterol export and Ebola infection. *Elife* **4**, e12177 (Dec 8, 2015).
26. A. I. Rosenbaum, F. R. Maxfield, Niemann-Pick type C disease: molecular mechanisms and potential therapeutic approaches. *Journal of neurochemistry* **116**, 789 (2011).
27. A. I. Rosenbaum *et al.*, Thiadiazole carbamates: potent inhibitors of lysosomal acid lipase and potential Niemann− Pick type C disease therapeutics. *Journal of medicinal chemistry* **53**, 5281 (Jul 22, 2010).
28. H. R. Sloan, D. S. Fredrickson, Enzyme deficiency in cholesteryl ester storage disease. *Journal of Clinical Investigation* **51**, 1923 (1972).
29. N. Beckmann, D. Sharma, E. Gulbins, K. A. Becker, B. Edelmann, Inhibition of acid sphingomyelinase by tricyclic antidepressants and analogons. *Frontiers in physiology* **5**, 331 (2014).
30. D. Roxbury *et al.*, Hyperspectral Microscopy of Near-Infrared Fluorescence Enables 17-Chirality Carbon Nanotube Imaging. *Sci Rep-Uk* **5**, 14167 (Sep 21, 2015).
31. R. Gref *et al.*, The controlled intravenous delivery of drugs using PEG-coated sterically stabilized nanospheres. *Adv Drug Deliver Rev* **64**, 316 (2012).
32. L. Illum, S. Davis, R. Müller, E. Mak, P. West, The organ distribution and circulation time of intravenously injected colloidal carriers sterically stabilized with a blockcopolymer-poloxamine 908. *Life sciences* **40**, 367 (1987).
33. D. E. Owens, N. A. Peppas, Opsonization, biodistribution, and pharmacokinetics of polymeric nanoparticles. *International journal of pharmaceutics* **307**, 93 (2006).
34. R. Gref *et al.*, Biodegradable long-circulating polymeric nanospheres. *Science* **263**, 1600 (1994).
35. Z. Liu *et al.*, Circulation and long-term fate of functionalized, biocompatible single-walled carbon nanotubes in mice probed by Raman spectroscopy. *Proceedings of the National Academy of Sciences* **105**, 1410 (Feb 5, 2008).
36. M. L. Schipper *et al.*, A pilot toxicology study of single-walled carbon nanotubes in a small sample of mice. *Nat Nanotechnol* **3**, 216 (Apr, 2008).
37. N. M. Iverson *et al.*, In vivo biosensing via tissue-localizable near-infrared-fluorescent single-walled carbon nanotubes. *Nat Nanotechnol* **8**, 873 (Nov, 2013).
38. K. Horinouchil, S. Erlichl, D. P. Perlz, K. Ferlinz, C. L. Bisgaier, Acid sphingomyelinase deficient mice: a model of types A and B. *Nature genetics* **10**, (1995).
39. M. Praggastis *et al.*, A murine Niemann-Pick C1 I1061T knock-in model recapitulates the pathological features of the most prevalent human disease allele. *Journal of Neuroscience* **35**, 8091 (2015).
40. J. D. Harvey *et al.*, A carbon nanotube reporter of microRNA hybridization events in vivo. *Nature Biomedical Engineering* **1**, 0041 (2017).

41. L. J. Dixon, C. A. Flask, B. G. Papouchado, A. E. Feldstein, L. E. Nagy, Caspase-1 as a central regulator of high fat diet-induced non-alcoholic steatohepatitis. *PloS one* **8**, e56100 (Feb 7, 2013).
42. L. H. Tetri, M. Basaranoglu, E. M. Brunt, L. M. Yerian, B. A. Neuschwander-Tetri, Severe NAFLD with hepatic necroinflammatory changes in mice fed trans fats and a high-fructose corn syrup equivalent. *American Journal of Physiology-Gastrointestinal and Liver Physiology* **295**, G987 (Nov, 2008).
43. H. Nagai, S. Toyokuni, Differences and similarities between carbon nanotubes and asbestos fibers during mesothelial carcinogenesis: shedding light on fiber entry mechanism. *Cancer science* **103**, 1378 (2012).
44. Z. Gao, J. A. Varela, L. Groc, B. Lounis, L. Cognet, Toward the suppression of cellular toxicity from single-walled carbon nanotubes. *Biomaterials science* **4**, 230 (2016).
45. W. Zhu *et al.*, Nanomechanical mechanism for lipid bilayer damage induced by carbon nanotubes confined in intracellular vesicles. *Proceedings of the National Academy of Sciences* **113**, 12374 (2016).
46. J. Budhathoki-Uprety, R. E. Langenbacher, P. V. Jena, D. Roxbury, D. A. Heller, A Carbon Nanotube Optical Sensor Reports Nuclear Entry via a Noncanonical Pathway. *Acs Nano* **11**, 3875 (2017).
47. E. T. Baronas, J.-W. Lee, C. Alden, F. Y. Hsieh, Biomarkers to monitor drug-induced phospholipidosis. *Toxicology and applied pharmacology* **218**, 72 (2007).
48. T. Van Berkel, Y. De Rijke, J. Kruijt, Different fate in vivo of oxidatively modified low density lipoprotein and acetylated low density lipoprotein in rats. Recognition by various scavenger receptors on Kupffer and endothelial liver cells. *Journal of Biological Chemistry* **266**, 2282 (1991).
49. G. Ao, M. Zheng, Preparation and separation of DNA-wrapped carbon nanotubes. *Curr Protoc Chem Biol* **7**, 43 (Mar 02, 2015).
50. D. Roxbury, A. Jagota, J. Mittal, Sequence-specific self-stitching motif of short single-stranded DNA on a single-walled carbon nanotube. *J Am Chem Soc* **133**, 13545 (2011).
51. D. Roxbury, J. Mittal, A. Jagota, Molecular-basis of single-walled carbon nanotube recognition by single-stranded DNA. *Nano Lett* **12**, 1464 (2012).
52. Y. Sugita, Y. Okamoto, Replica-exchange molecular dynamics method for protein folding. *Chemical physics letters* **314**, 141 (1999).
53. W. L. Jorgensen, J. Chandrasekhar, J. D. Madura, R. W. Impey, M. L. Klein, Comparison of simple potential functions for simulating liquid water. *The Journal of chemical physics* **79**, 926 (1983).
54. W. Humphrey, A. Dalke, K. Schulten, VMD: visual molecular dynamics. *Journal of molecular graphics* **14**, 33 (1996).
55. I. Mederacke, D. H. Dapito, S. Affò, H. Uchinami, R. F. Schwabe, High-yield and high-purity isolation of hepatic stellate cells from normal and fibrotic mouse livers. *Nature protocols* **10**, 305 (2015).

Acknowledgments: This work was supported in part by the NIH New Innovator Award (DP2-HD075698), the Cancer Center Support Grant (P30 CA008748), NIHNS081981 (D.S.O.) the Honorable Tina Brozman Foundation for Ovarian Cancer Research, the Expect Miracles Foundation - Financial Services Against Cancer, the Anna Fuller Fund, the Louis V. Gerstner Jr. Young Investigator's Fund, the Frank A. Howard Scholars Program, Cycle for Survival, the Alan and Sandra Gerry Metastasis Research Initiative, Mr. William H. Goodwin and Mrs. Alice Goodwin and the Commonwealth Foundation for Cancer Research, the Experimental Therapeutics Center, the Imaging & Radiation Sciences Program, the Pershing Square Sohn Cancer Research Alliance and the Center for Molecular Imaging and Nanotechnology of

Memorial Sloan Kettering Cancer. J.M. was supported by the U.S. Department of Energy (DOE), Office of Science, Basic Energy Sciences (BES) under award DE-SC0013979. D.R. was supported by the American Cancer Society Roaring Fork Valley Postdoctoral Fellowship (PF-13-388801-TBG. P.V.J was supported by an NIH NCI T-32 fellowship (2T32CA062948-21). T.V.G. was supported by the Frank Lappin Horsfall Jr. Fellowship.

Supplementary Materials:

Materials and Methods

Figures S1-S18

Supplementary Materials for

In Vivo Reporter of Endolysosomal Lipids Reveals Enduring Effects of Diet on Hepatic Macrophages

Thomas V. Galassi[1,2], Prakrit V. Jena[1], Janki Shah[1], Geyou Ao[3], Elizabeth Molitor[4], Yaron Bram[2], Angela Frankel[2], Jiwoon Park[2], Jose Jessurun[2], Daniel S. Ory[4], Adriana Haimovitz-Friedman[1], Daniel Roxbury[5], Jeetain Mittal[6], Ming Zheng[3], Robert E. Schwartz[2], Daniel A. Heller[1,2*]

[1]Memorial Sloan Kettering Cancer Center, New York, NY 10065

[2]Weill Cornell Medical College, New York, NY 10065

[3]National Institute of Standards and Technology, Gaithersburg, MD 20899

[4]Department of Medicine, Washington University School of Medicine, St. Louis, MO 63110

[5]Department of Chemical Engineering, University of Rhode Island, Kingston, RI 02881

[6]Department of Chemical and Biomolecular Engineering, Lehigh University, Bethlehem, PA 18015

Correspondence to: hellerd@mskcc.org

This PDF file includes:

Materials and Methods

DNA encapsulation of single-walled carbon nanotubes:
EG 150X single-walled carbon nanotubes (SWCNT) were purchased from Chasm Advanced Materials (Norman, Oklahoma). Aqueous dispersions of SWCNTs in ssDNA were produced *via* probe tip ultrasonication (Sonics & Materials, Inc.) of raw 2 mg/mL ssDNA with 1 mg/mL raw SWCNT powder in 0.1 mol/L NaCl for 120 min at 8 W. Following sonication aqueous dispersions were centrifuged (Eppendorf 5430 R) for 90 min at 17,000 x g. The top 85 % of the resulting supernatant was then collected and used for chirality enrichment.

Isolation of single nanotube chiralities:
The (9,4) SWCNT was purified from unsorted samples of ssCTTC$_3$TTC-SWCNT using the aqueous two phase separation method (*20, 22, 49*). ssCTTC$_3$TTC-SWCNT was mixed with a solution containing a final concentration of 7.76% polyethylene glycol (PEG, molecular mass 6 kDa, Alfa Aesar), and 15.0 % polyacrylamide (PAM, molecular mass 10 kDa, Sigma Aldrich). The sample was then incubated overnight at room temperature, vortexed, and centrifuged at 10,000 x g for 3 min. The top phase was then collected and added to blank "bottom phase," which was produced by centrifuging a 7.76 % PEG, 15.0 % PAM solution at 10,000 x g for 10 min and then removing the bottom phase of solution. The resulting solution was then vortexed and centrifuged, and the top phase, which contained highly enriched ssCTTC$_3$TTC-(9,4) was collected. NaSCN was added to the collected top phase at a final concentration of 0.5 mol/L and the resulting solution was incubated overnight to precipitate ssCTTC$_3$TTC-(9,4). The sample was then centrifuged at 17,000 x g for 20 min which causes ssCTTC$_3$TTC-(9,4) to pellet. The resulting supernatant was then removed and the pellet was re-suspended in dH_2O and stored with 0.1 mg/mL free ssCTTC$_3$TTC for stability.

Hyperspectral microscopy of cells and resected tissue sections:
Hyperspectral microscopy (*30*) was performed by injecting a continuous wave 730 nm diode laser (output power = 2 W), into a multimode fiber to provide an excitation source for experiments. Homogenous illumination over the field of view was assured by passing the excitation beam through a custom beam shaping module to produce a top hat intensity profile with a maximum of 20 % variation on the surface of the sample. The laser was reflected into an Olympus IX-71 inverted microscope (with internal optics modified for near infrared transmission) equipped with a 100X (UAPON100XOTIRF, NA=1.49) oil objective (Olympus, USA) *via* a longpass dichroic mirror with a cut-on wavelength of 880 nm. Spatially resolved near-infrared emission from the sample passed through a volume Bragg grating (VBG) so that it could be spectrally defined. Following its passage through the VBG, a specific wavelength component of emitted polychromatic light was diffracted, while all other wavelengths were transmitted through the grating. The diffracted component then passed through the VBG a second time resulting in a monochromatic beam which was collected by a 256 x 320 pixel InGaAs array (Photon Etc.). This method was used to obtain a continuous stack of images for specified wavelength ranges which resulted in hyperspectral cubes wherein every pixel of a near-infrared image was spectrally resolved (*30*).

Analysis and processing of hyperspectral data:
Acquired hyperspectral data was saved as 16 bit arrays (320 x 256 x Y), where the first two coordinates represent the spatial location of a pixel and the last coordinate its position in wavelength space (in this study Y ranged from (26 to 125). For data taken on purified samples of the (9,4) or (7,6) nanotube a 26 frame wavelength space that ranged from (1100 to 1200) nm was used. A peak finding algorithm was used to determine the intensity range for a given pixel *i.e.* range = (intensity_maximum – intensity_minimum). Data points were designated as peaks if their intensity was range/4 greater than the intensity of adjacent pixels. Pixels that did not meet this threshold (primarily due to low signal above background) were removed from data sets. Remaining pixels were fit with a Lorentzian function.

Photoluminescence plots and fluorescence spectroscopy of nanotubes in solution:
Photoluminescent excitation/emission spectra of ssDNA-SWCNTs were acquired using an assembly consisting of a SuperK EXTREME supercontinuum white light laser source (NKT photonics), inverted microscope, and InGaAs near-infrared detector. The excitation source was used with a Varia variable bandpass filter accessory capable of tuning the output from (490 to 825) nm with a bandwidth of 20 nm. The excitation beam was filtered with a long pass dichroic mirror with a cut on wavelength of 900 nm. Excitation light was shaped and fed into the back of an inverted IX-71 microscope (Olympus) and passed through a 20X near-infrared objective (Olympus LCPlan N 0.45 IR) to illuminate 100 µL aqueous sample of nanotubes at a concentration of 0.2 mg/L (sorted nanotube samples) or 1.0

mg/L (unsorted nanotube samples). Emission light was collected through the 20X objective, passed through a dichroic mirror (875 nm, Semrock), and f/# matched to an Isoplane SCT-320 spectrograph (f/4.6, Princeton Instruments) with a slit width of 410 µm. Emission light was dispersed with a 86 g/mm grating with a blaze wavelength of 950 nm and collected by a NIRvana 640 x 512 pixel InGaAs array (Princeton Instruments). Following acquisition, spectral corrections for wavelength-dependent excitation power, non-linearity in the InGaAs detector response, and background subtraction were applied to data. For fluorescence spectroscopy measurements at a single excitation wavelength, a continuous wave laser with an output power of 1 W was used as the excitation source. This laser emitted at 730 nm, which is close to the resonant excitation maximum of ssCTTC$_3$TTC-(9,4).

Near infrared, *in vivo* spectroscopy:
Non-invasive *in vivo* spectra were taken using a custom-built reflectance probe-based spectroscopy system (*40*). Excitation light was provided by injecting a continuous wave 730 nm diode laser (Frankfurt) into a bifurcated fiber optic reflection probe bundle (Thorlabs). The sample leg of the bundle included one 200 µm, 0.22 NA fiber optic cable for sample excitation located in the center of six 200 µm, 0.22 NA fiber optic cables for collection of the emitted light. Excitation power at the sample was 590 mW with a 1 cm circle being illuminated. An exposure time of 5 s was used for all *in vivo* data acquisition. Long pass filters were used to filter emission light below 1050 nm, and emission light was focused through a 410 µm slit into a Czerny-Turner spectrograph with 303 mm focal length (Shamrock 303i, Andor). Emission light was dispersed by an 85 g/mm grating with 1350 blaze wavelength and collected by an iDus InGaAs camera (Andor). Following acquisition data was processed to apply spectral corrections for non-linearity of the InGaAs detector response, background subtraction, and baseline subtraction *via* the use of OriginPro 9 software with a standard adjacent averaging smoothing method and a spline interpolation method. Center wavelengths were determined by fitting processed spectra to a Lorentzian function.

Quantification of ssCTTC$_3$TTC-(9,4) biodistribution *ex vivo*:
ssCTTC$_3$TTC-(9,4) fluorescence from the liver, lung, heart, kidneys, and spleen was measured *ex vivo* using the instrument described in the preceding paragraph. Following acquisition, data was processed to apply spectral corrections for non-linearity of the InGaAs detector response, background subtraction, and baseline subtraction *via* the use of OriginPro 9 software with a standard adjacent averaging smoothing method and a spline interpolation method. The integrated intensity was then determined by calculating the area under the curve from (1080 to1180) nm with OrginPro 9 software. Integrated intensities were then normalized by dividing by the maximum value obtained for all measurements.

Fluorescence imaging of SWCNT *in vivo* an *ex vivo*:
Fluorescence imaging of SWCNT *in vivo* and *ex vivo* was performed using a preclinical hyperspectral mouse imaging system (Photon Etc., Montreal). Excitation was provided by two continuous wave 730 nm diode lasers each with an output power of 2 W. Lasers were reflected off optical mirrors and distributed over the entire mouse with a maximum power density of 340 mW/cm^2. Emission light was filtered through an 1100 nm longpass filter to reduce autofluorescence. Intensity maps of SWCNT emission were produced by first creating a binary mask of images based off of intensity thresholding. For hyperspectral animal imaging, light was passed through a volume Bragg grating (VBG) as described in the "hyperspectral microscopy of cells and resected tissue sections" section.

Analysis and processing of *in vivo* and *ex vivo* fluorescence images:
In vivo hyperspectral cubes were processed as described in the section above titled "analysis and processing of hyperspectral data." *In vivo* and *ex vivo* fluorescence images were processed using ImageJ 1.48v. After image acquisition, background subtraction was performed using the "image calculator" function of ImageJ. Binary masks were then created *via* an intensity threshold method to excluded background noise from images. Masks were then multiplied by fluorescence images to produce intensity profiles which were overlaid on white light images.

Nanotube chirality and DNA sequence-dependent response to LDL:
Sorted DNA-SWCNT samples were diluted to 0.2 mg/L in PBS and incubated with 0.5 mg/mL low-density lipoprotein (LDL, Alfa Aesar) for 6 h at room temperature. Controls were incubated with no LDL present. Photoluminescent spectra were acquired with 0.5 s exposure time.

DNA-nanotube response to acidic pH:

Phosphate buffered saline was mixed in a 1:1 ratio with a glacial-acetate buffer (final buffer strength was 10 mmol/L) to allow a wide range of pH levels to be obtained. HCl and NaOH were used to titrate solutions at pH 5.4 and 7.2. Unsorted ssCTTC$_3$TTC-SWCNT was incubated in each solution for 18 hours at 37 degrees Celsius. Photoluminescent plots of DNA-SWCNT were then taken with a two second exposure time allowing ssCTTC$_3$TTC-(9,4) to be spectrally resolved.

Response of ssCTTC$_3$TTC-(9,4) to near saturating concentrations of biomolecules:
ssCTTC$_3$TTC-(9,4) samples at a concentration of 0.4 mg/L were incubated in cell culture media (Dulbecco's modified Eagle media with 1% penicillin/streptomycin, and 1 % glutamine) with 1 % fetal bovine serum (Gibco) for 90 min at RT to allow for the acquisition of a protein corona. Samples were then mixed in a 1:1 ratio with bovine serum albumin (final concentration = 20 mg/mL), salmon testes dsDNA (final concentration = 1 mg/mL), or carboxymethyl cellulose (final concentration = 5 mg/mL). Samples were incubated for 18 h at RT and spectra were taken with 730 nm excitation.

Titration of ssCTTC$_3$TTC-(9,4) with PEG-conjugated lipids:
ssCTTC$_3$TTC-(9,4) samples at a concentration of 0.4 mg/L were incubated in cell culture media (Dulbecco's modified Eagle media with 1% penicillin/streptomycin, and 1% glutamine) with 1% fetal bovine serum (Gibco) for 90 min at RT to allow for the acquisition of a protein corona. Samples were then mixed in a 1:1 ratio with solutions of varying concentrations of lipids solubilized *via* conjugation with either polyethylene glycol (PEG) or methoxy-PEG, so that the final concentration of ssCTTC$_3$TTC-(9,4) in solution was 0.2 mg/L. The following PEG-conjugated lipids were used: Cholesterol-PEG 600, "PEG-Cholesterol", (Sigma Aldrich); C16 PEG750 Ceramide, "PEG-Ceramide", (Avanti Lipids); and 18:0 PEG550 PE, "mPEG-PE 18:0", (Avanti Lipids). Samples were incubated for 18 hours at 37 degrees Celsius. PEG and mPEG, with molecular weights of 600, 550, and 750 were used as controls to test for non-specific interactions. The concentrations of PEG and mPEG used matched the highest concentrations used for the PEG-lipid sensing experiment.

ssCTTC$_3$TTC-(9,4) response to U18666A, Lalistat 3a2, and imipramine *in vitro*:
ssCTTC$_3$TTC-(9,4) was incubated at a concentration of 0.2 mg/L in complete cell culture media with 10% fetal bovine serum alone or with U18666A (3 µg/mL), Lalistat 3a2 (10 µmol/L), or imipramine hydrochloride (10 µmol/L) for 18 h at RT. Spectra were then taken with 730 nm excitation as described previously.

Cell culture and reagents:
RAW 264.7 TIB-71 cells (ATCC, Manassas, VA) were grown at 37 degrees Celsius and 5 % CO_2 in sterile, filtered Dulbecco's modified Eagle media (DMEM) with 10 % fetal bovine serum (heat inactivated) 2.5 % HEPES, 1% glutamine, and 1 % penicillin/streptomycin. For 100X imaging, cells were plated on glass bottom petri dishes (MatTek). All cells were used at (70 to 80) % confluence.

Reporter validation in live cells:
Cells were treated with U18666A (3 µg/mL), Lalistat 3a2 (10 µmol/L), or imipramine hydrochloride (10 µmol/L) for 24 h to allow for endolysosomal lipid accumulation to occur. Control cells were untreated. Following the 24 h treatment period, nanotubes were added at 0.2 mg/L to fresh culture media and incubated with cells for 30 min at RT. Cells were then washed and media replaced to remove SWCNTs that had not been internalized during the 30 min incubation. Data was acquired *via* hyperspectral imaging 6 h after SWCNT incubation.

Molecular dynamics simulations:
All-atom replica exchange molecular dynamics (REMD) simulations (*50 to 52*) were performed to understand the interactions between a carbon nanotube, single-stranded DNA, sphingomyelin, and cholesterol. Four strands of ssCTTC$_3$TTC DNA were placed in a desorbed state in the vicinity of a 4.757 nm long SWCNT with a (9,4) chirality. The DNA and SWCNT were solvated in a 5 x 5 x 4.757 nm water-box containing approximately 3,300 TIP3P model (*53*) water molecules and sodium counter-ions, placed randomly, to balance the negative charges from phosphates on DNA (fig. S6). The total system was 11,500 atoms. The SWCNT extended to the edge of the water box. The SWCNT atoms were modeled as sp^2 hybridized carbon. All structures were visualized in VMD (*54*).

To run the REMD simulations, the Gromacs 4.6.7 simulation package was used with the Charmm36 force field. Long-range electrostatics were calculated using the particle mesh Ewald method with a 0.9 nm real space cutoff. For

van der Waals interactions, a cutoff value of 1.2 nm was used. The DNA-SWCNT configuration was energy minimized and subjected to 100 ps equilibration (NVT) at 300 K. Forty replicas were created with temperatures ranging from 300 K to 585 K. Temperature intervals increased with absolute temperature to maintain uniform exchange probability. The 40 replicas were run in parallel for 300 ns of NVT production. Exchange between adjacent temperature replicas was attempted every 2 ps and the temperature list was optimized to ensure that the acceptance ratio remained at least 20 %. The time step of the simulation was 2 fs. The trajectories were saved every 10 ps, yielding a total of 30,000 snapshots for production analysis. For clustering, solvent accessibility, water density, and hydrogen bonding analysis, the 300 K trajectory was used.

Three molecules of sphingomyelin or 5 molecules of cholesterol (chosen to keep atom density approximately the same) were evenly distributed in the water-box of the top equilibrium cluster of the ssCTTC$_3$TTC + (9,4) configuration (fig. S6). This configuration served at the initial configurations for the combination simulations (DNA + sphingomyelin or DNA + cholesterol). The system was again energy-minimized, heated for 100 ps (NVT), and replicated in temperature space. The configurations were then run for an additional 200 ns of NVT production (hence 300 times through 500 ns of total simulated time). Again, the 300 K trajectory was used for subsequent analysis. The simulation time totaled ([300 ns x 40] + 2*[200 ns x 40]) = 0.028 ms.

Clustering of the REMD trajectory is useful to determine the underlying equilibrium structures in the simulated configuration. Here, we used a native Gromacs clustering function (g_cluster) with a root mean square deviation **(**RMSD) cutoff of 0.8 nm based upon the positions of the DNA backbone atoms. The top cluster from the 30,000 available snapshots represented 21.4 % of the total 300 K trajectory. We found significant inter-strand and intra-strand DNA interactions in the top cluster. In agreement with previous studies (*50, 51*), the DNA remained bound to the SWCNT throughout the duration of the simulation.

The solvent accessibility was analyzed using the Gromacs function 'g_sas'. In the ssCTTC$_3$TTC + (9,4) configuration, it was clear that the DNA evolved to wrap the SWCNT from its initially unbound state, and shield the SWCNT from solvent (water or sodium) molecules (fig. S7). The addition of the sphingomyelin or cholesterol molecules in the subsequent simulations further decreased the solvent accessibility to the SWCNT surface. Although the solvent accessibility to surface molecules decreased, there were significant changes in water density. This reflects the hydrophobic nature of sphingomyelin-water and cholesterol-water interfaces rather than steric constraint. This data is in agreement with a decrease in water density found near the surface of the SWCNT in the ssCTTC$_3$TTC + sphingomeylin + (9,4) and ssCTTC$_3$TTC + cholesterol + (9,4) configurations (Fig. 1 main text).

Hydrogen bonding analysis was performed using the Gromacs function 'g_hbond'. In the ssCTTC$_3$TTC + (9,4) configuration, there was a significant increase in the number of DNA-DNA hydrogen bonds as the DNA adsorbed onto the SWCNT and adopted an equilibrium arrangement (fig. S7). Similar analyses were performed for the ssCTTC$_3$TTC + sphingomeylin + (9,4) and ssCTTC$_3$TTC + cholesterol + (9,4) configurations (fig. S7).

Animal studies:
All animal studies were approved by and carried out in accordance with the Memorial Sloan Kettering Cancer Center Institutional Animal Care and Use committee. Male C57BL/6 mice were purchased from Jackson Laboratories (Bar Harbor, ME), at age (4 to 8) weeks of age. For observing ssCTTC$_3$TTC-SWCNT removal from blood, 6 week old male SKH1-Elite mice were purchased from Charles River Laboratories. Mice for the acid sphingomyelinase knockout experiment were graciously provided by the Schuchman Laboratory (Mount Sinai) (*38*) and used at 5 months of age. NPC1 I1061T and wild type controls were bred in the lab of D.O. and experiments were performed when mice were 10 weeks of age. All control and experimental mice were age matched and housed in identical environments. For *in vivo* sensing experiments mice were tail vein injected with 200 µL of 1.0 mg/L ssCTTC$_3$TTC-(9,4) diluted in PBS. For the hepatic cell isolation experiments 18 mg/L of unsorted ssCTTC$_3$TTC eg150X SWCNT was injected. For *in vivo* imaging and spectroscopy mice were anesthetized with 2 % isoflurane prior to data collection. Exposure time for spectroscopy was 5 s, while exposure times for *in vivo* imaging ranged from 0.5 s for broadband imaging to 10 min for hyperspectral imaging.

ssCTTC$_3$TTC-SWCNT removal from blood:
200 µL of a 50 mg/L solution of ssCTTC$_3$TTC-SWCNT was injected into male SKH1-Elite mice (6 weeks old) that were purchased from Charles River Laboratory. Immediately following injection movies of mice were taken with the aforementioned preclinical mouse imaging system to determine the fluorescence in different regions of the mice.

Images of mice were then taken periodically to quantify the fluorescence signal over the long term. Fluorescence intensity was quantified in three regions of interest (ROIs) for each mouse by drawing ROIs over white light images of the mice as shown in Figure 2 of the main text.

Diet:
"Western diet (WD)" mice were given an adjusted calorie diet ad libitum. This diet was purchased from Envigo (formerly Harlan Laboratories) and contained 42 % calories from fat. By weight the diet contained 17.3 % protein, 48.5 % carbohydrate, 21.2 % fat and 0.2 % cholesterol (.05 % from fat source, .15 % added). Full details on the diet (TD88137) can be found here: http://dybiotech.skyd.co.kr/images/ath/88137.pdf. Water was supplemented with 42 g/L of high fructose corn syrup equivalent which consisted of 55 % fructose and 45 % glucose by mass (*42*). All other mice received standard chow and water ad libitum.

Tissue fixation and sectioning:
Mouse organs were fixed in 10 % buffered formalin phosphate and paraffin embedded before 5 µm sections were placed on glass slides. Paraffin was removed and the slides were stained with haematoxylin and eosin (H&E) for basic histology at the Molecular Cytology Core Facility of Memorial Sloan Kettering Cancer Center and Histowiz Inc (Brooklyn, NY). For frozen tissue sections a small piece of liver tissue was placed in an optical cutting temperature (OCT, Tissue-Tek) formulation for ten minutes and then transferred to a mold containing OCT. The mold with tissue was then placed into a stainless steel beaker of 2-methylbutane that has been cooled in liquid nitrogen. After the OCT had solidified completely, the block was removed from the 2-methylbutane and placed on dry ice or in a -20°C cryostat. Five micron sections were placed on glass slides. Thirty minutes later slides were washed with phosphate buffered saline. Finally slides were covered with a cover slip and then imaged.

Transmission electron microscopy:
Liver tissue was rinsed with PBS and then cut into 5 mm cubes. Cubes were placed in a modified Karnovsky's fix of 2.5 % glutaraldehyde, 4 % parafomaldehye and 0.02 % picric acid in 0.1mol/L sodium caocdylate buffer for sixty minutes. Following a secondary fixation in 1 % osmium tetroxide, 1.5 % potassium ferricyanide, samples were dehydrated through a graded ethanol series, and embedded in an epon analog resin. Ultrathin sections were cut ((55 to 60) nm) using a Diatome diamond knife (Diatome, USA, Hatfield, PA) on a Leica Ultracut T ultramicrotome (Leica Microsystems, Wetzlar, Germany). Sections were then placed on copper grids, contrasted with lead citrate and viewed on a JEM 1400 electron microscope (JEOL, USA, Inc., Peabody, MA) operated at 100 kV. Images were recorded with a Veleta 2K x 2K CCD camera (Olympus-SIS, Germany).

Atomic force microscopy:
A stock solution (2.5 mg/L in PBS) of ssCTTC$_3$TTC-(9,4) was diluted 1:5 in a buffer consisting of 20 mM HEPES (pH 6.8) and 5 mmol/L $MgCl_2$. 40 µl of this solution was plated on freshly cleaved mica substrate (SPI) for 30 min before washing with 10 mL of Molecular Biology Grade H_2O (Fisher BP2819-1) and blown dry with nitrogen gas. Imaging was performed using a Cypher S AFM (Asylum Research), with an Olympus AC240TS-R3 AFM probe (Asylum Research) in tapping mode at room temperature. Images were captured for length distribution measurements at a scan size of 2µm x 2µm (1024 x 1024), as well as an overview image at 6µm x 6µm (2048 x 2048).

Hepatic cell isolation:
C57BL/6 mice purchased from Jackson Laboratories (Bar Harbor, ME), at age (6 to 8) weeks of age. Mouse hepatocytes were harvested *via* a two-step in situ collagenase perfusion technique modified from Seglen. Briefly, mice were anesthetized using isofluorane. The portal vein was cannulized, and *in vivo* perfusion (5 mL/min X 10 min) was performed with a calcium-free hydroxyethylpiperazineethanesulfonic acid (HEPES)-buffered solution (143 mmol/L NaCl, 6.7 mmol/L KCl, 10 mM HEPES, 100 mg % ethylene glycol-bis-aminoethyl ether (EGTA; Sigma, St. Louis, MO), pH 7.4), and then perfused (5 mL/min X 10 min) with a second HEPES-buffered solution (, pH 7.6) containing 0.05 % collagenase D (Roche Corp., Indianapolis, IN). The liver was then resected and placed in isolation medium [Williams' E medium (GIBCO, Grand Island, NY) with 10,000 U/liter penicillin G, 100 mg/liter streptomycin sulfate]. The liver capsule was peeled back from all lobes, and the liver was then gently combed to isolate hepatocytes. The hepatocyte pellet was resuspended in isolation medium following gauze filtration and centrifuged at 50 g for 10 min. The cells were then resuspended and placed on top of Percoll gradient and hepatocyte fraction was isolated. The

nonparenchymal cell was further processed. F4/80 labeling was completed and the F4/80 positive population was sorted and plated down on tissue culture treated plastic for further analysis.
HSC were isolated using in situ digestion protocol as described in (*55*). In brief pronase/collagenase perfusion of mouse liver was performed with subsequent *in vitro* digestion; and density gradient–based separation of HSCs from other hepatic cell populations. FACS was then performed to ensure HSC purity by obtained the Violet bright population.

Statistics:
GraphPad Prism versions 6.02 and 7 were used to perform statistical analysis. All data met the assumptions of the statistical tests performed (*i.e.* normality, equal variances, *etc*.). The F-test and Brown-Forsythe tests were used to determine if variance was similar between groups for t-tests, and one way ANOVAs, respectively. The testing of multiple hypotheses was accounted for by performing one way ANOVAs with Dunnet's Tukey's or Sidak's post tests when appropriate. Sample sizes were determined based off of the authors' previous experiences with experimental equipment which show minimal instrumental noise.

Code availability
Matlab code for any of the analyses included in this manuscript are available upon request, by contacting the corresponding author on the manuscript, hellerd@mskcc.org.

Supplementary Text

Identification of ssCTTC$_3$TTC-(9,4) as a potential probe for endolysosomal lipid accumulation: The ability of four different purified, DNA-sequence, nanotube chirality combinations to detect lipids in the endolysosomal lumen was investigated. Tested DNA sequence-nanotube chirality combinations included ssCTC$_3$TC-(7,6), ssT$_3$C$_5$T$_3$-(7,6), ssT$_2$C$_4$T$_2$-(9,4), and ssCTTC$_3$TTC-(9,4). To test the sensitivity of each combination to lipid molecules their emission wavelength was measured following a 6 h incubation with 0.5 mg/mL low-density lipoprotein (LDL) at RT (fig. S2). As all of the tested DNA sequence-nanotube chirality combinations displayed sensitivity to lipids (fig. S2), the ability of each to detect lipids from within the endolysosomal lumen was investigated. RAW 264.7 macrophages were treated for 24 h with 3 μg/mL U18666A to cause endolysosomal lipid accumulation and then incubated with the aforementioned DNA sequence-nanotube combinations as described in the materials and methods section. Six hours after nanotube addition to media hyperspectral microscopy was performed on cells. Of each of the tested combinations, ssCTTC$_3$TTC-(9,4) exhibited the greatest change in emission wavelength between control and U18666A treated RAW cells (fig. S2).

ssCTTC$_3$TTC-SWCNT removal from blood:
To assess the short term biodistribution of ssCTTC$_3$TTC-SWCNT, 200 μL of a 50 mg/L solution was injected into SKH1-Elite mice (6 weeks old) that were purchased from Charles River Laboratory. A higher concentration of SWCNT was used here to ensure signal could be seen within the circulation of the mice. SKH1 mice were used because their hairless nature aids in the imaging process. Immediately following injection, movies of mice were taken with the aforementioned preclinical mouse imaging system to determine the fluorescence intensity in different regions of the mice. Images of mice were then taken periodically to quantify the fluorescence signal over the long term. Fluorescence intensity was quantified in three regions of interest (ROIs) for each mouse by drawing ROIs over white light images of the mice as shown in Figure 2 of the main text. Results showed that immediately after injection SWCNT signal increased in all three ROIs, but then decreased in the upper and lower ROIs while remaining relatively constant in the middle ROI which contained the liver (Fig. 2A, main text). After 5 min almost all fluorescent signal came from this ROI (Fig. 2A, main text). Over the next 6 hours the fluorescence signal in this ROI decreased (Fig. 2A, main text), potentially due to SWCNT being trafficked from the liver vasculature into Kupffer cell lysosomes. The signal was then relatively stable from (24 to 72) h post injection, although it was decreasing slightly over that time frame (Fig. 2A, main text).

Assessment of the effect ssCTTC$_3$TTC-(9,4) on liver histology and blood chemistry:
A pathologist observing hematoxylin and eosin stained liver sections of reporter injected and control mice found that the reporter injection did not alter liver pathology of mice fed standard chow or the Western diet for three months. (fig. S15). To further assess the effect of ssCTTC$_3$TTC-(9,4) injection after twenty four hours, serum chemistry measurements were performed on reporter injected and control mice fed standard chow or the western diet for three

months. Between injected and control mice no statistically significant differences were found for the liver injury markers aspartate aminotransferase (AST), alanine aminotransferase (ALT), AST:ALT, lactate dehydrogenase (LDH), alkaline phosphatase (ALP), globulin (GLOB), or albumin (ALB):GLOB (fig. S17). While ALB and total protein levels were significantly different between control and injected standard chow mice, the levels in the injected mice were actually slightly increased compared to control mice (low, rather than high, levels of ALB and total protein may be indicative of a liver disorder) (fig. S17). Moreover, although statistically significant the actual difference in the levels for ALB and total protein between the two groups was slight (fig. S17).

When observing serum chemistry levels in mice fed the western diet for three months no significant differences were seen in the levels of AST, AST:ALT, ALB, GLOB, ALB:GLOB, or total protein between control and injected mice (fig. S17). While statistically significant differences were seen in the levels of ALT, LDH, and ALP between control and injected mice, these differences would suggest increased liver injury in control, rather than injected mice (fig. S17). We believe that these differences are most likely related to the increased weight of mice from the un-injected control group. This weight disparity between the two groups is almost certainly random as mice were placed into groups randomly and we find it very unlikely that injection of the reporter significantly alters the weight of a mouse in only 24 h.

Hyperspectral imaging and analysis of ssCTTC$_3$TTC-SWCNT uptake in isolated hepatic cells:
Kupffer cells and hepatocytes were isolated from C57BL/6 mice that were injected intravenously with ssCTTC$_3$TTC-SWCNT as described in the supplementary methods section. Transmitted light, broad-band and hyperspectral images were obtained from cells and emission in each image was summed from 1100-1300 nm to calculate the total near-infrared emission from each pixel in an image. For each cell we calculated the mean nanotube emission intensity per cell, and normalized this to the average nanotube emission intensity in Kupffer cells as these cells exhibited the highest amount of SWCNT uptake. To assess SWCNT uptake in hepatic stellate cells C57BL/6 mice were injected with ssCTTC$_3$TTC-SWCNT and their livers pooled to allow for isolation of hepatic stellate cells as described in the supplementary methods section. Imaging was performed on hepatic stellate cells as described above. For comparison, imaging was also performed on unsorted hepatic cells from the same mice. In total, hyperspectral images were taken of forty-eight individual cells (which all had morphologies and SWCNT uptake similar to what was seen in the sorted Kupffer cell images) present in the unsorted cell mixture that exhibited SWCNT uptake. To control for potential differences in the tail vein injections, the SWCNT intensity from within hepatic stellate cells was normalized by the intensity of the cells in the unsorted plate that showed SWCNT uptake. This normalized intensity per cell is presented in Figure 2E.

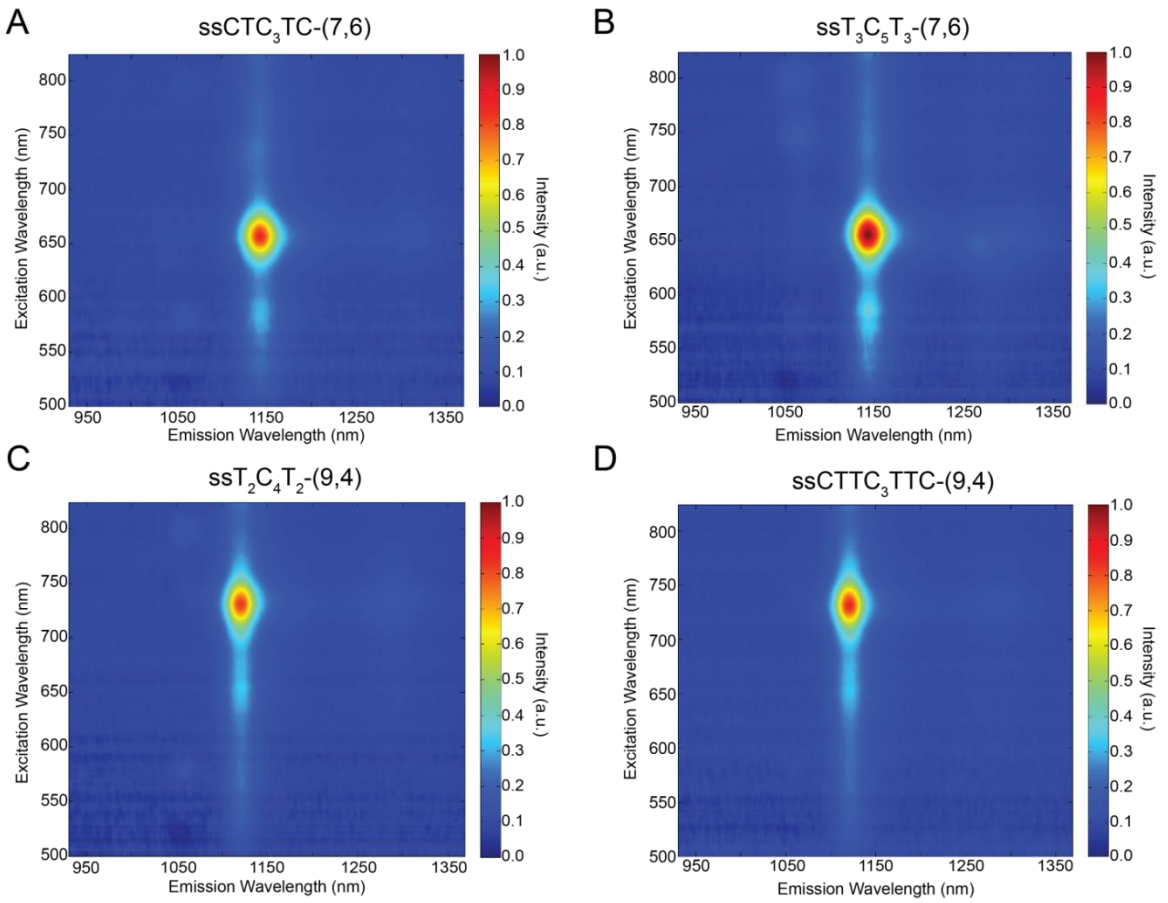

Fig. S1

Two-dimensional photoluminescence (PL) plots of isolated single-walled carbon nanotube (SWCNT) chiralities, non-covalently complexed with single stranded (ss) DNA and purified *via* the aqueous two phase polymer separation method (*22*). **(A)** PL plot of the (7,6) SWCNT non-covalently complexed with ssCTC$_3$TC. **(B)** PL plot of the (7,6) SWCNT non-covalently complexed with ssT$_3$C$_5$T$_3$. **(C)** PL plot of the (9,4) SWCNT non-covalently complexed with ssT$_2$C$_4$T$_2$. **(D)** PL plot of the (9,4) SWCNT non-covalently complexed with ssCTTC$_3$TTC.

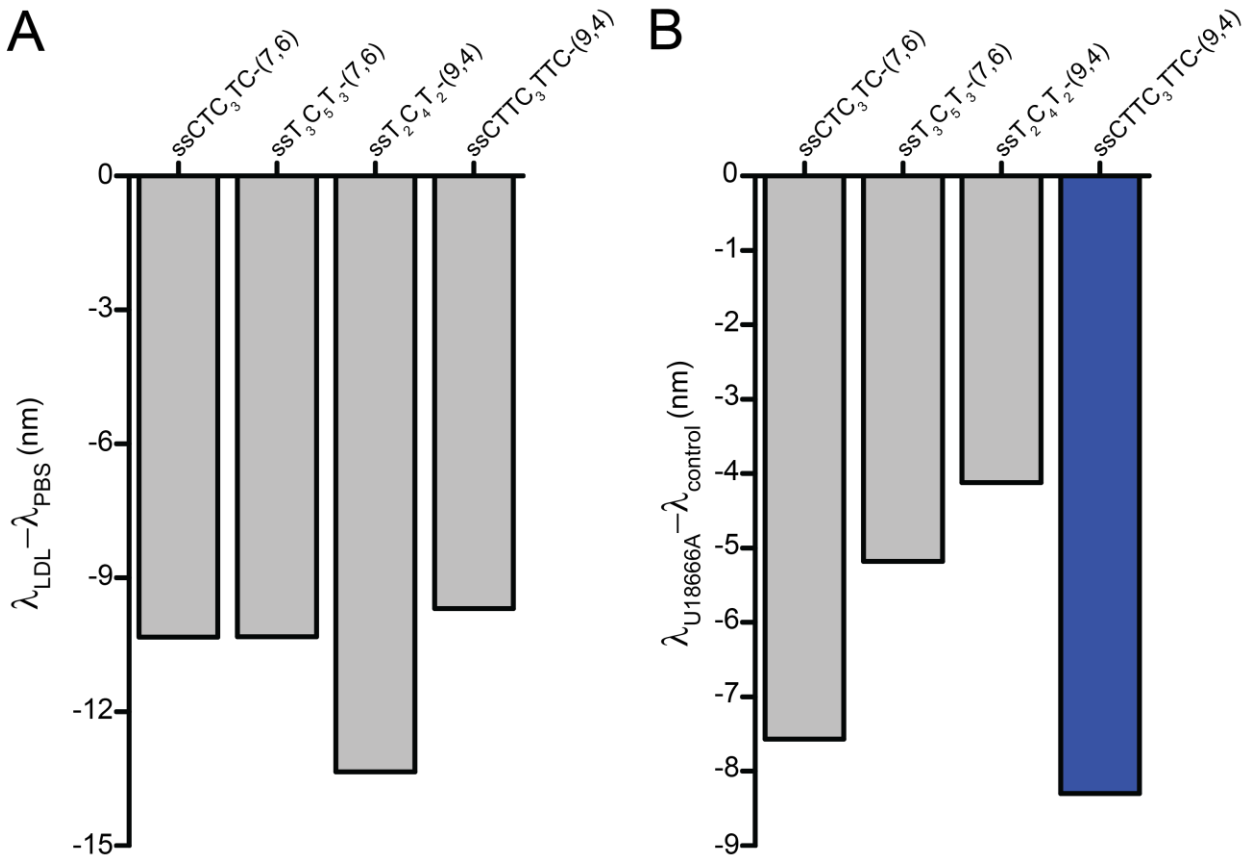

Fig. S2
Identification of ssCTTC$_3$TTC-(9,4) as a potential probe for endolysosomal lipid accumulation. **(A)** Photoluminescent response of DNA-nanotube complexes to 0.5 mg/mL low density lipoprotein in solution following a 6 h incubation at RT. **(B)** Emission wavelength of ssCTTC$_3$TTC-(9,4) in RAW 264.7 macrophages cultured in the presence of U18666A (3µg/mL for 24 h) to force endolysosomal lipid accumulation compared to the emission wavelength seen from untreated control cells.

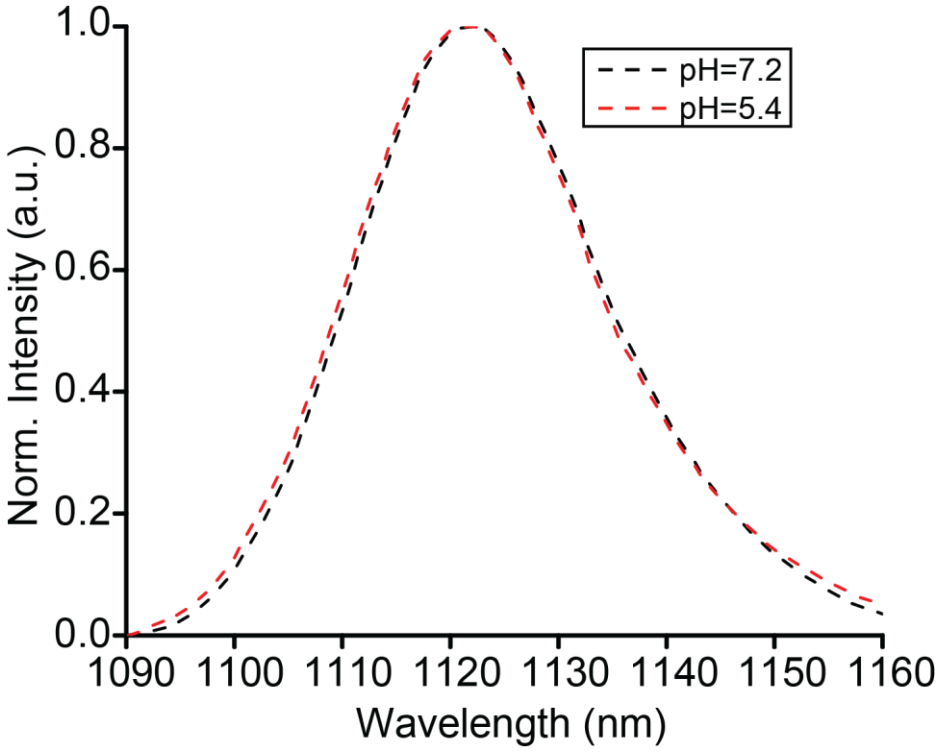

Fig. S3
Representative emission spectra of ssCTTC$_3$TTC-(9,4) at a neutral and acidic pH.

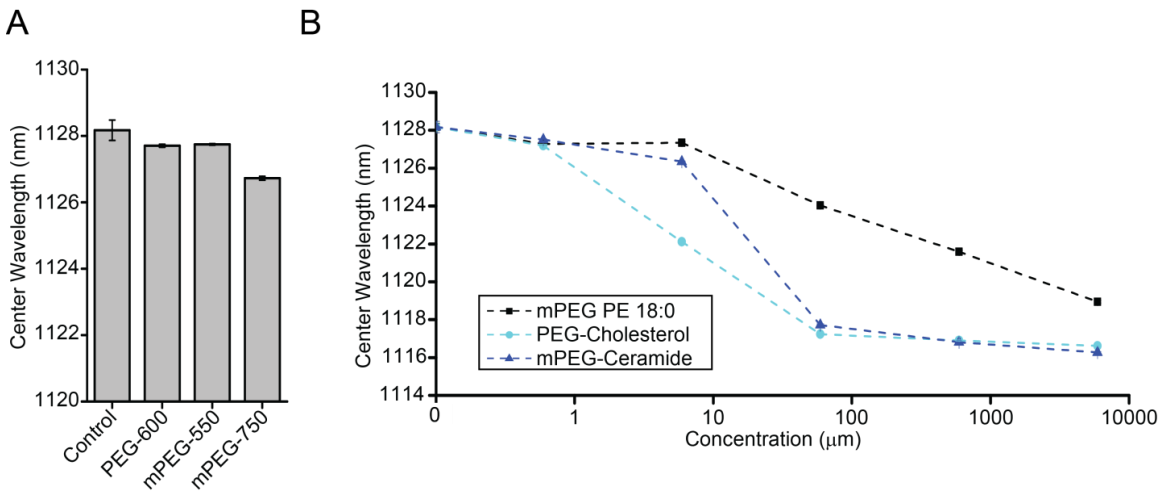

Fig. S4

ssCTTC$_3$TTC-(9,4) photoluminescent response in solution. **(A)** Emission wavelength of ssCTTC$_3$TTC-(9,4) in response to PEG and mPEG molecules. Concentrations of PEG/mPEG represented here are equal to the concentrations of PEG/mPEG used to solubilize the PEGylated lipids represented in Figure 1 of the main text. **(B)** Photoluminescent response of ssCTTC$_3$TTC-(9,4) to increasing concentrations of PEG-cholesterol, mPEG-ceramide and mPEG-phosphoethanolamine 18:0 (mPEG-PE 18:0). Error bar stands for one standard deviation.

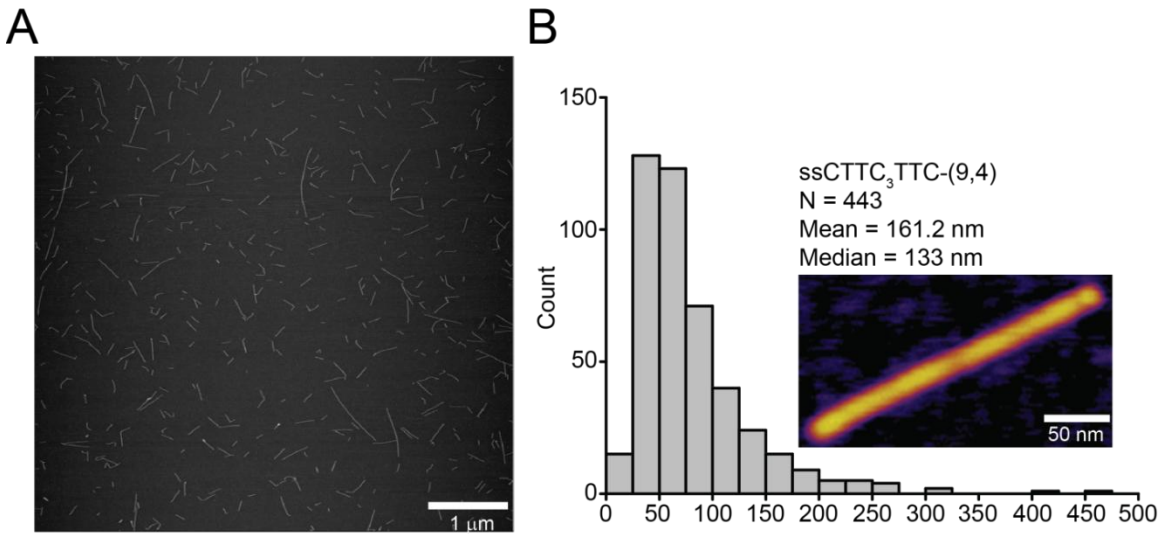

Fig. S5

Atomic force microscopy (AFM) of ssCTTC$_3$TTC-(9,4) complexes. **(A)** AFM image of ssCTTC$_3$TTC-(9,4) deposited on a surface. **(B)** Length distribution of ssCTTC$_3$TTC-(9,4) as quantified from AFM images, with a high resolution image of a ssCTTC$_3$TTC-(9,4) complex (inset).

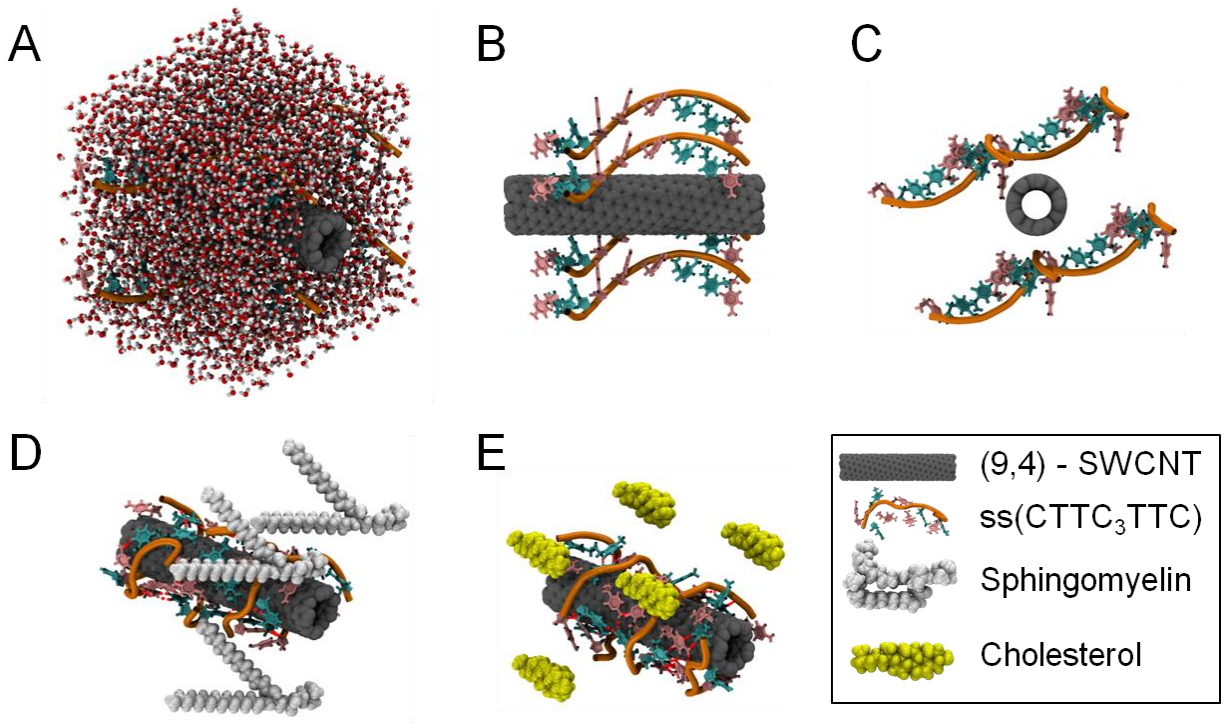

Fig. S6
Initial replica exchange molecular dynamics (REMD) configurations. **(A)** Starting configuration of the ssCTTC$_3$TTC DNA oligonucleotide with the (9,4) nanotube species shown in an explicit water box with counter-ions. **(B)** Side view of the ssCTTC$_3$TTC + (9,4) nanotube shown with water and ions removed. **(C)** Similar configuration shown edge-on. **(D)** Starting configuration of the ssCTTC$_3$TTC-(9,4) nanotube complex in the presence of sphingomyelin. **(E)** Similar starting configuration in the presence of cholesterol.

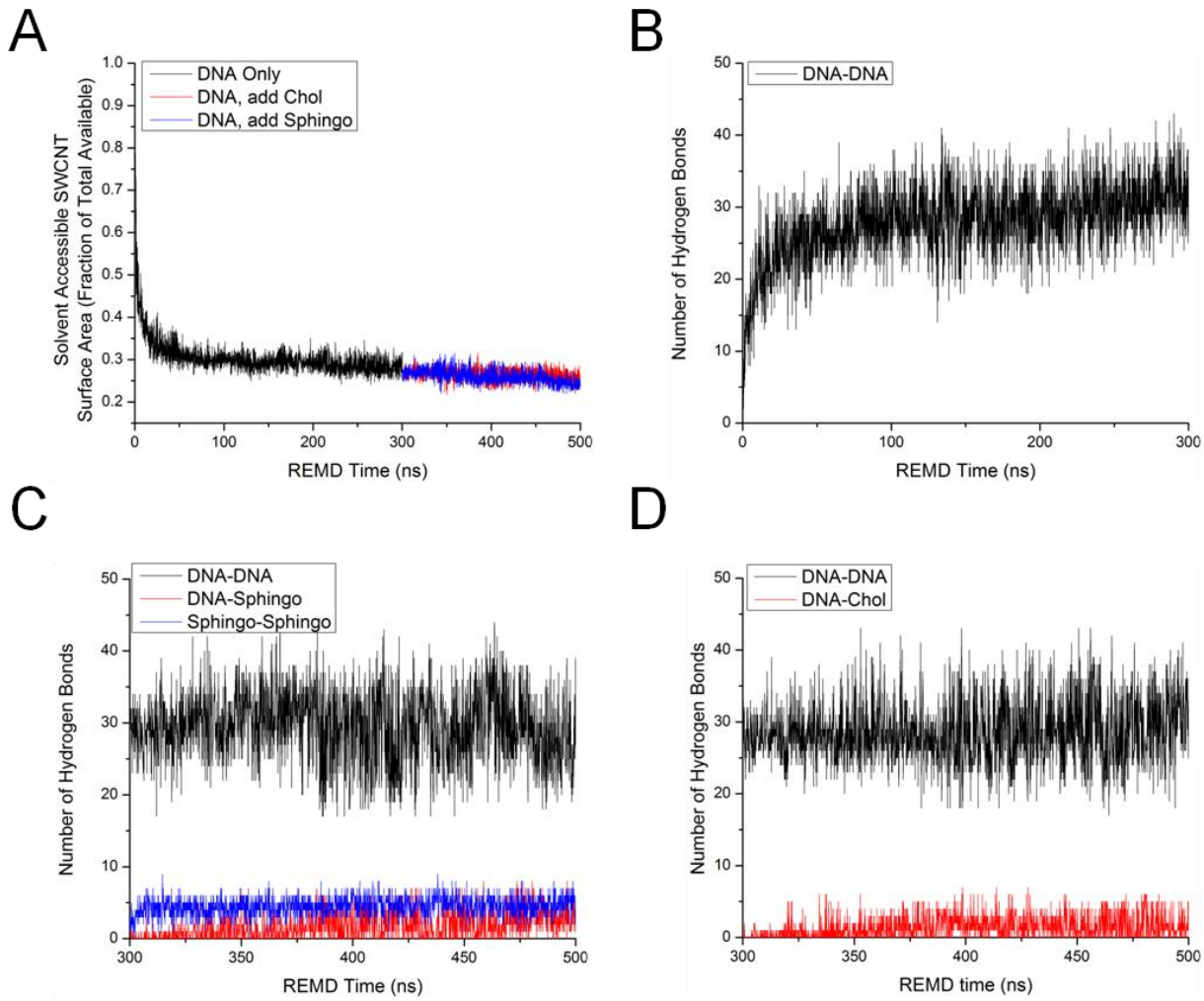

Fig. S7

Analysis of REMD simulations. **(A)** Solvent accessible SWCNT surface area vs. simulation time for the three simulated configurations (DNA only, DNA + cholesterol, and DNA + sphingomyelin). **(B)** Number of hydrogen bonds between DNA strands vs. simulation time for the ssCTTC$_3$TTC + (9,4) configuration. **(C)** Number of DNA-DNA, DNA-sphingomyelin, and sphingomyelin-sphingomyelin hydrogen bonds in the ssCTTC$_3$TTC-(9,4) nanotube + sphingomyelin configuration. **(D)** Similar hydrogen bond analysis for the ssCTTC$_3$TTC-(9,4) nanotube + cholesterol configuration.

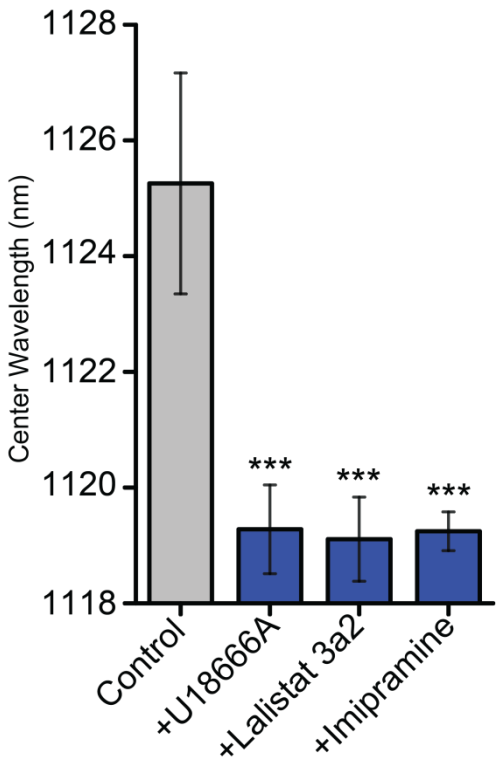

Fig. S8
Mean emission wavelength of ssCTTC$_3$TTC-(9,4) in live RAW 264.7 macrophages that have been treated with U18666A (3 µg/mL), Lalistat 3a2 (10 µmol/L), or imipramine hydrochloride (10 µmol/L) for twenty-four hours. ***=p<.001 compared to control as determined with a one-way ANOVA with Dunnet's multiple comparison test (N=7 for control, 3 for all other groups). Error bars represent standard deviation.

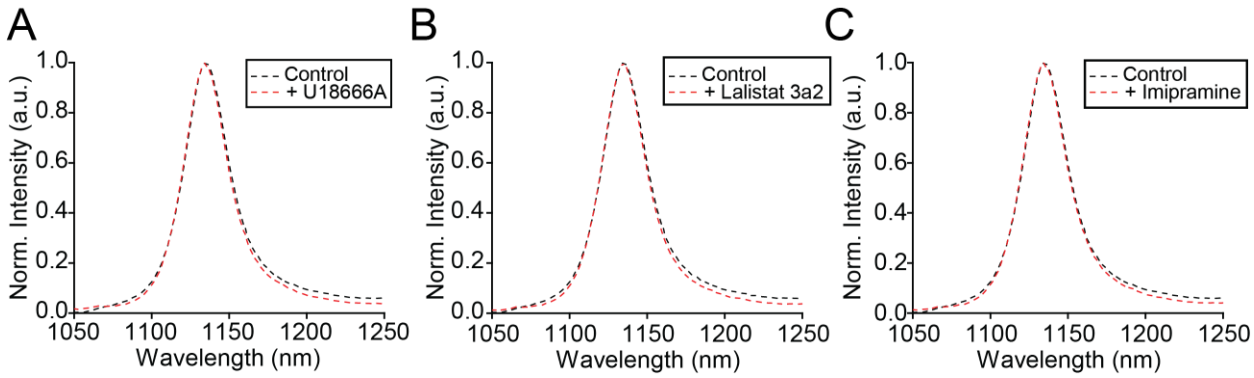

Fig. S9

Effect of inhibitors on ssCTTC$_3$TTC-(9,4) emission spectra in solution. **(A)** Representative emission spectra of ssCTTC$_3$TTC-(9,4) in solution alone and after incubation with 3 µg/mL U18666A at RT for 18 h. **(B)** Representative emission spectra of ssCTTC$_3$TTC-(9,4) in solution alone and after incubation with 10 µmol/L Lalistat 3a2 at RT for 18 h. **(C)** Representative emission spectra of ssCTTC$_3$TTC-(9,4) in solution alone and after incubation with 10 µmol/L imipramine hydrochloride at RT for 18 h.

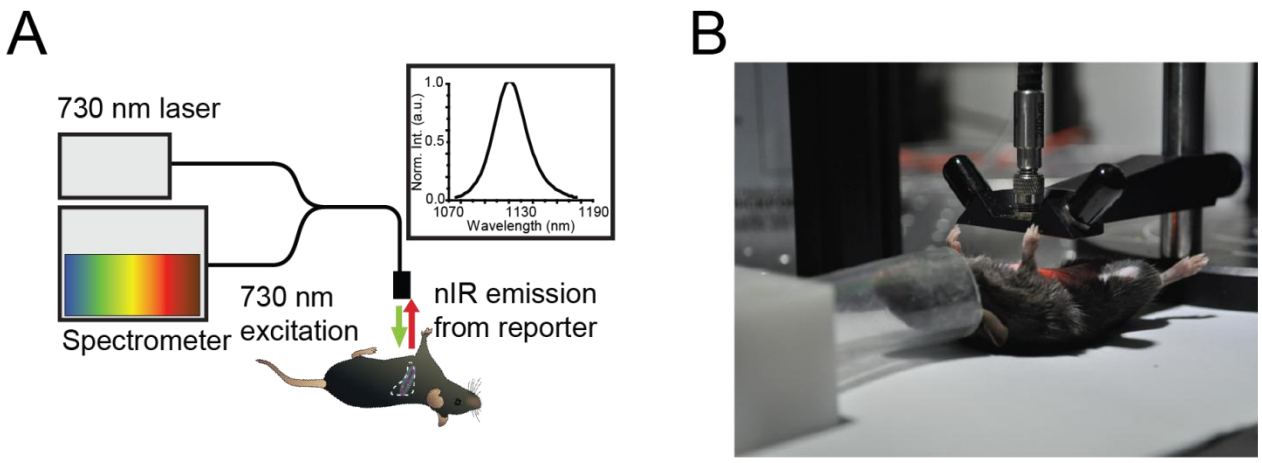

Fig. S10
Near-infrared *in vivo* spectroscope. **(A)** Schematic of the near-infrared, *in vivo* spectroscope used for the non-invasive detection of ssCTTC$_3$TTC-(9,4) from the liver *in vivo*. A spectra obtained after intravenous injection with 200 ng ssCTTC$_3$TTC-(9,4) is shown in the inset. **(B)** Photograph showing data acquisition from an anesthetized mouse using the *in vivo* spectroscope.

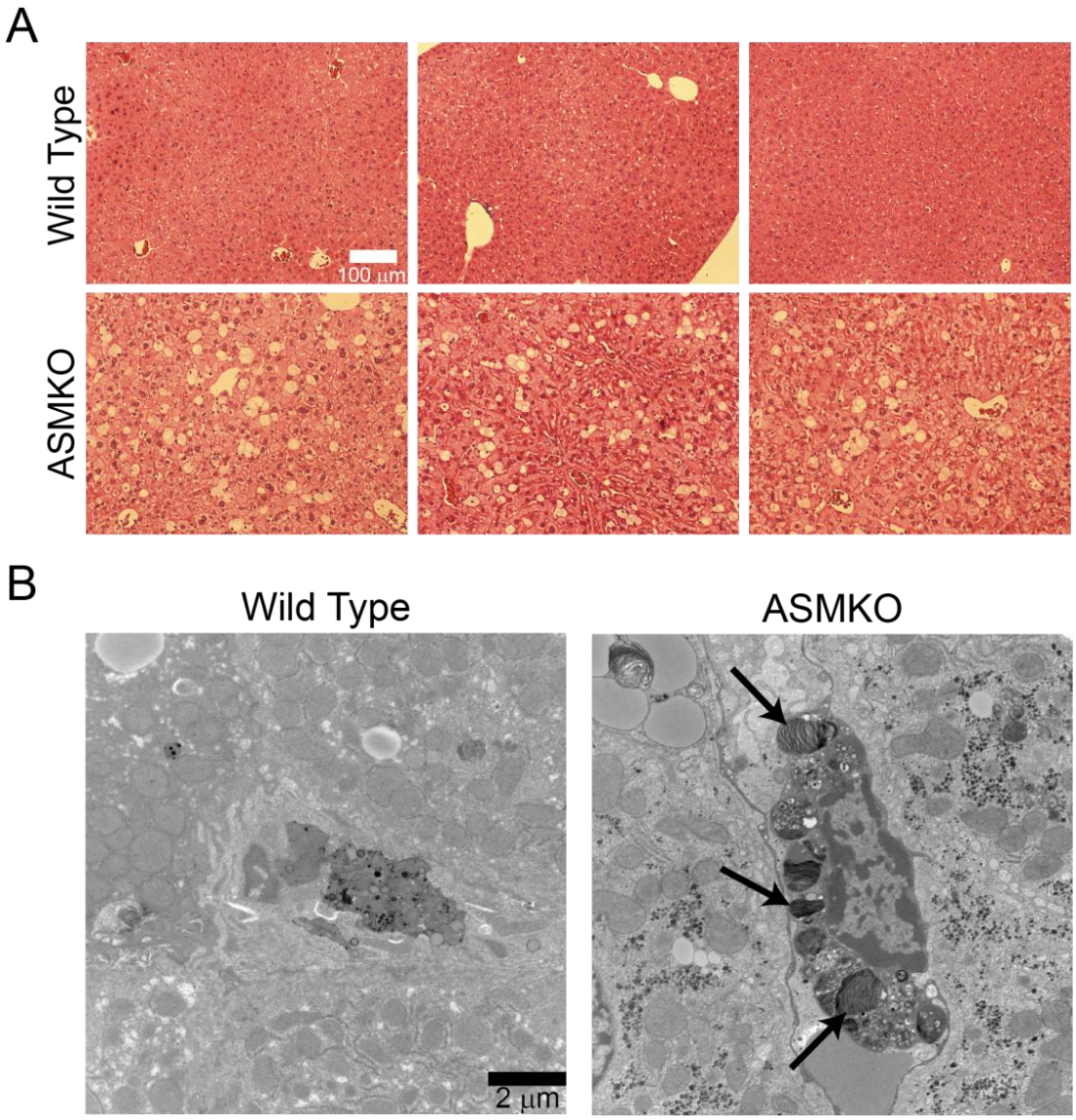

Fig. S11
Representative images of liver tissue from wild type and acid sphingomyelinase knockout (ASMKO) mice. **(A)** Representative hematoxylin and eosin stained images from the livers of wild type and ASMKO mice. Note the presence of "foamy" cells in ASMKO livers. **(B)** Representative transmission electron microscopy (TEM) images of liver tissue showing Kupffer cells from wild type and ASMKO mice. Note the presence of lipid laden lysosomes (arrows) from within the Kupffer cell of an ASMKO mouse.

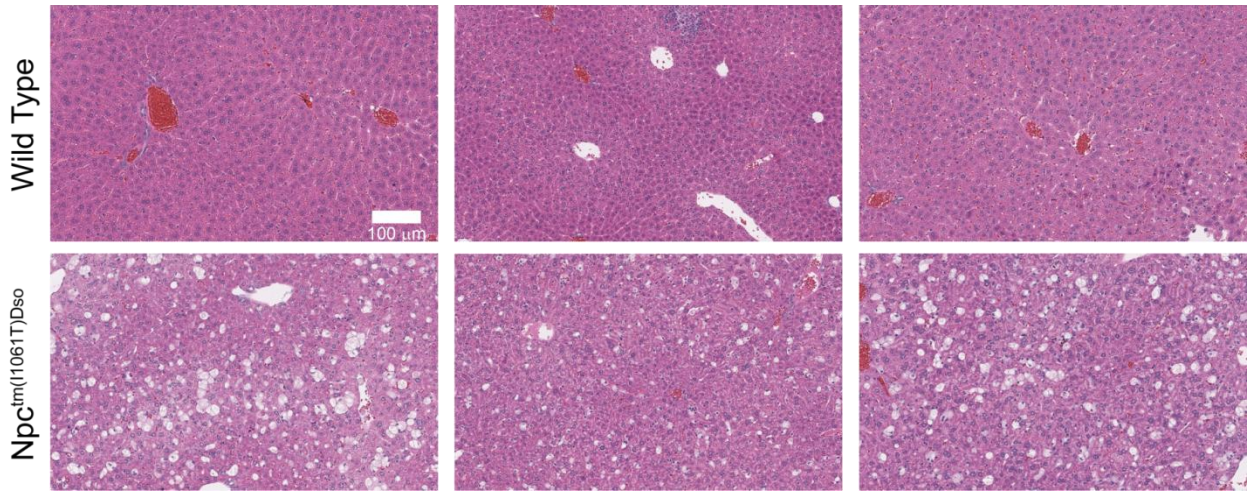

Fig. S12
Representative hematoxylin and eosin stained images from the livers of wild type and $Npc^{tm(I1061T)Dso}$ mice. Note the presence of "foamy" cells in $Npc^{tm(I1061T)Dso}$ livers.

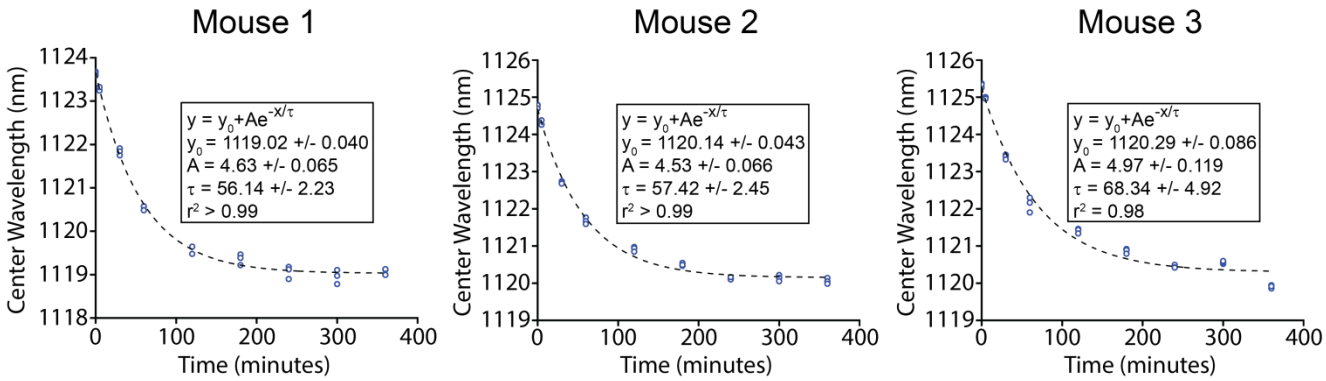

Fig. S13

Exponential fits of the decrease in ssCTTC$_3$TTC-(9,4) emission wavelength following intravenous injection of 200 µg of oxLDL. Fits are shown for three biological replicates, with multiple technical replicates taken for each time point.

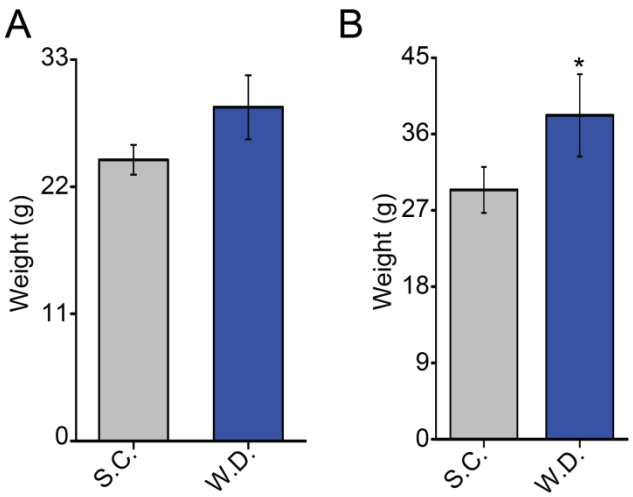

Fig. S14
Weights of male C57BL/6 mice fed standard chow (S.C.) or the Western diet (Envigo TD.88137) with high fructose corn syrup supplemented water (W.D.). **(A)** Weights of S.C. and W.D. mice after one month of feeding. **(B)** Weights of S.C. and W.D. mice after three months of feeding. *=p<.05 determined with a t-test with Welch's correction. Error bars represent standard deviation. N=3-4 per group mice for panel A, N=5 mice per group for panel B.

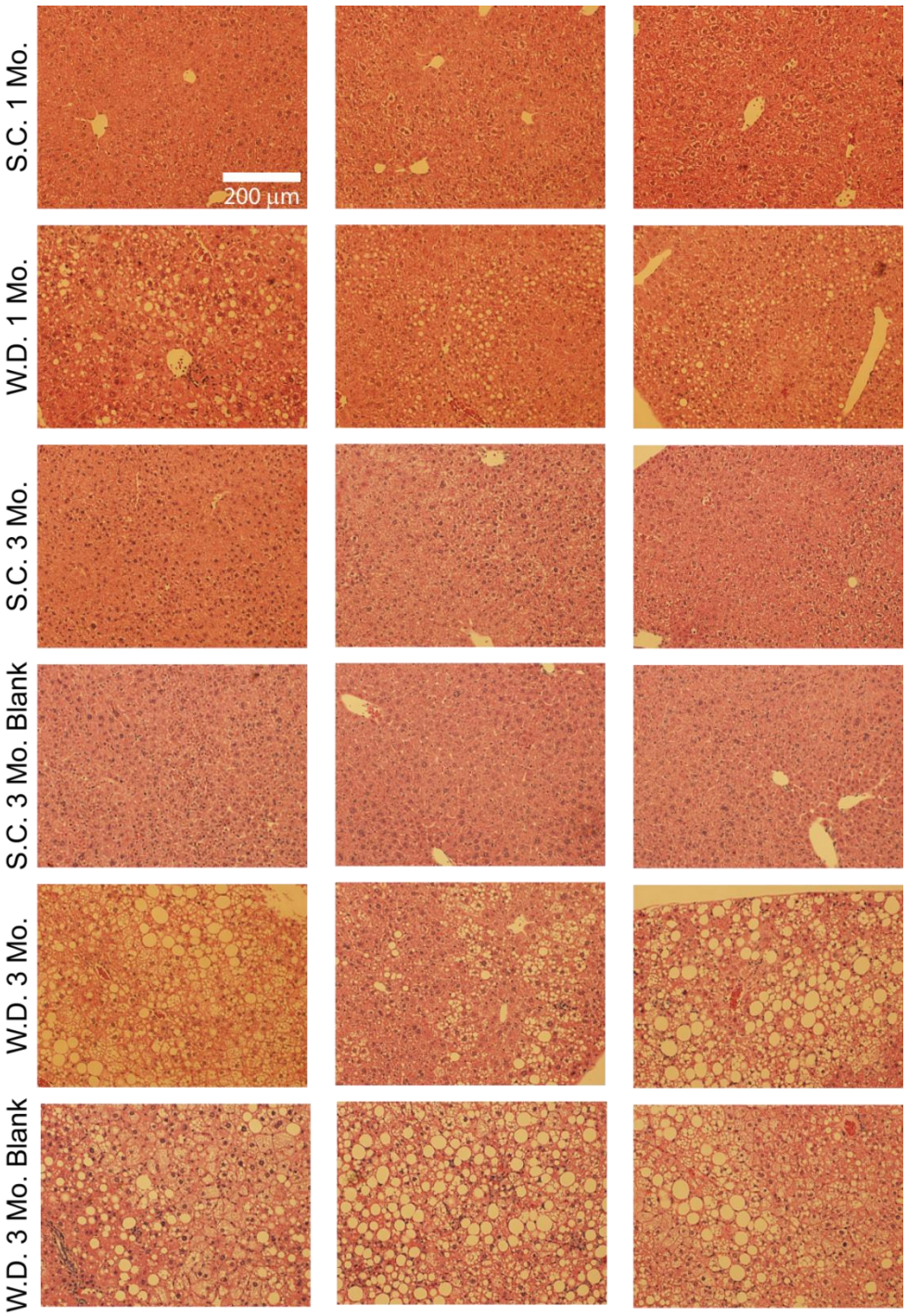

Fig. S15

Representative hematoxylin and eosin stained images of liver tissue from mice fed standard chow (S.C.) or the Western diet (Envigo TD.88137) with high fructose corn syrup supplemented water (W.D.) for 1 to 3 months (Mo.). "Blank" indicates these mice were not injected with ssCTTC$_3$TTC-(9,4), while other groups were injected intravenously with 200 ng of ssCTTC$_3$TTC-(9,4) twenty four hours prior to euthanization.

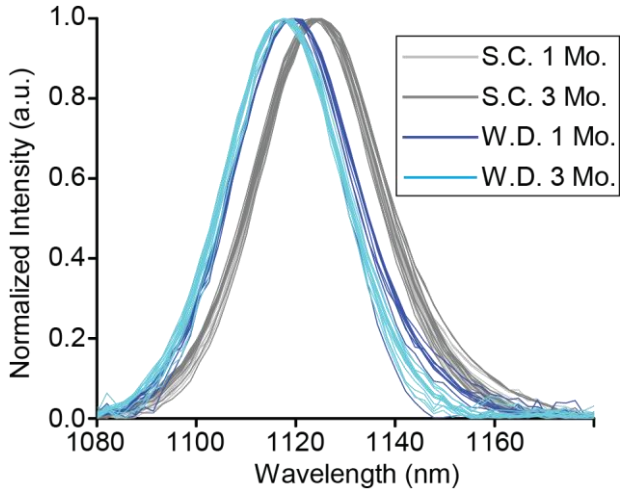

Fig. S16
Non-invasive, *in vivo* emission spectra of ssCTTC$_3$TTC-(9,4) from the liver of mice fed standard chow (S.C.) or the Western diet (Envigo TD.88137) with high fructose corn syrup supplemented water (W.D.) for 1 to 3 months (Mo.). Emission spectra were measured twenty four hours after intravenous injection of 200 ng ssCTTC$_3$TTC-(9,4). Spectra shown represent multiple technical replicates taken from (3 to 5) different biological replicates per group.

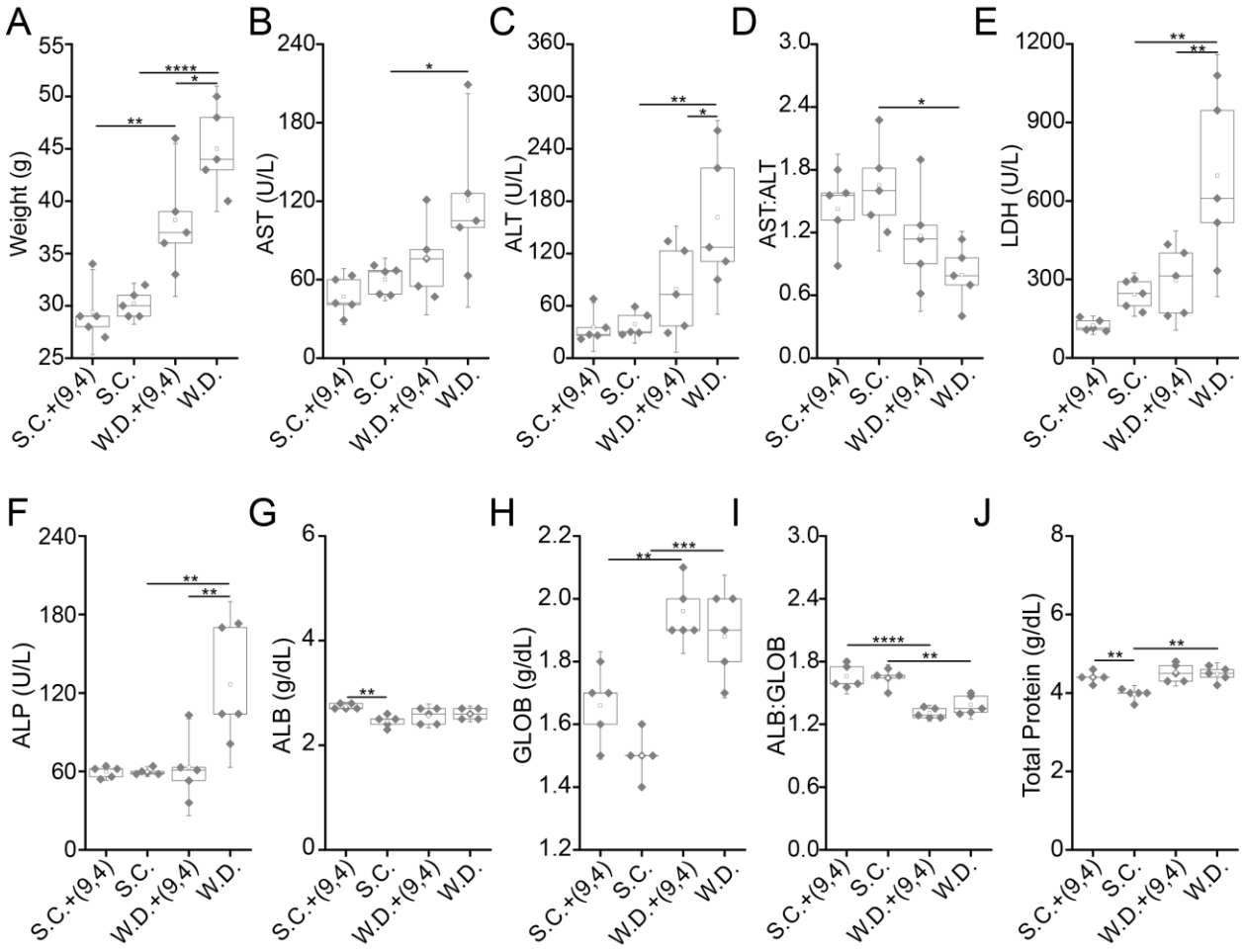

Fig. S17

Weight and serum chemistry measurements of mice fed standard chow (S.C.) or the Western diet (Envigo TD.88137) with high fructose corn syrup supplemented water (W.D.) for three months (Mo.). "+ (9,4)" indicates mice that were injected with 200 ng of ssCTTC$_3$TTC-(9,4) while other groups were un-injected. All measurements were taken twenty four hours after injection with ssCTTC$_3$TTC-(9,4). **(A)** Weight measurements of control and injected S.C. and W.D. mice after three months of feedings. **(B)** Serum aspartate transaminase (AST) levels in control and injected S.C. and W.D. mice. **(C)** Serum alanine transaminase levels (ALT) in control and injected S.C. and W.D. mice. **(D)** Serum AST:ALT ratio in control and injected S.C. and W.D. mice. **(E)** Serum lactate dehydrogenase (LDH) levels in control and injected S.C. and W.D. mice. **(F)** Serum alkaline phosphatase (ALP) levels in control and injected S.C. and W.D. mice. **(G)** Serum albumin (ALB) levels in control and injected S.C. and W.D. mice. **(H)** Serum globulin (GLOB) levels in control and injected S.C. and W.D. mice. **(I)** Serum ALB:GLOB ratio in control and injected S.C. and W.D. mice. **(J)** Serum total protein levels in control and injected S.C. and W.D. mice.

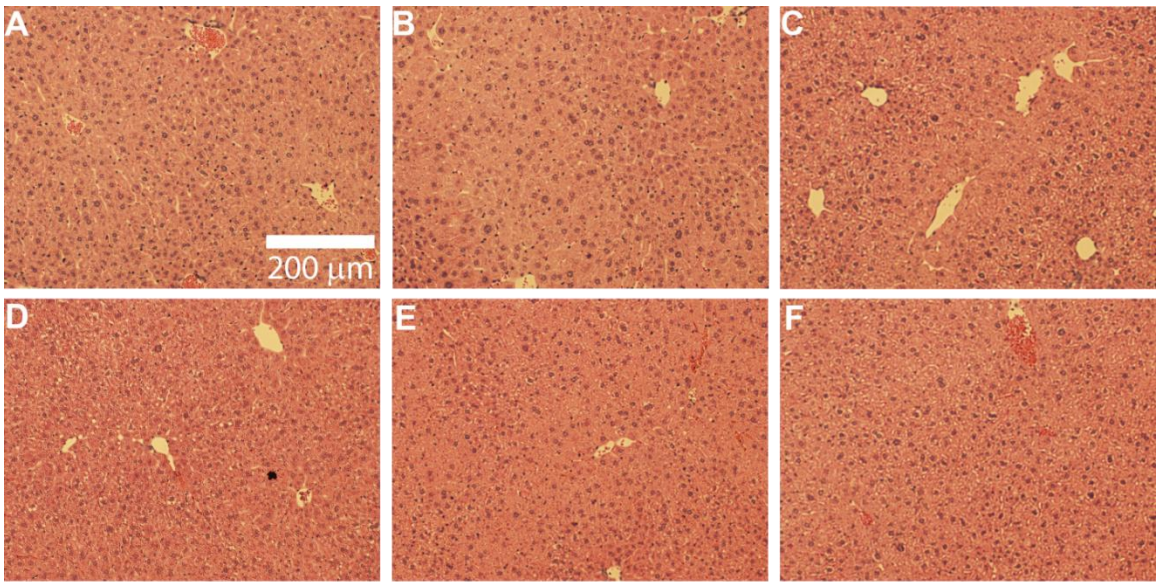

Group Details

A: S.C. for 2 weeks
B: S.C.- Age-matched control for (E)
C: S.C.- Age-matched control for (F)
D: W.D. for 2 weeks
E: W.D. for 2 weeks ⟶ S.C. 2 weeks
F: W.D. for 2 weeks ⟶ S.C. 6 weeks

Fig. S18
Representative H&E sections of livers from mice depicted in Figure 5E of the main text.